Session 1A1
Poster Session 1

An Improved Electrical Model of a Biological Cell Taking Electroporation into Account

N. Citro, **V. Tucci**, **B. de Vivo**, **and P. Lamberti**
University of Salerno, Italy

Electro-permeabilization of biological cells has been proposed as a very efficient pasteurization method in food technology, in biotechnology for gene transfer, in medicine for gene therapy, cancer chemotherapy, and drug delivery. Although the molecular processes involved in the permeabilization mechanisms are very complex, the formation of "pores" in the plasma membrane, under the influence of an electric field, is deemed responsible of the cellular responses. Electric field intensity and duration are the fundamental parameters in the modulation of the occurring phenomena. The effects of the application of an electric field can be evaluated by adopting either a lumped parameters circuital model or a continuous field based description of the cell structure. In both cases one of the main parameters affecting the cell response is the voltage across the membrane (trans-membrane voltage-TMV). If trans-membrane voltage is greater than a critical value, structural changes in the surface membrane occur that cause pore formation and, in turn, increased permeability. Recently, it has been shown that for pulses in the ns range, intracellular structures may be affected without appreciable modifications in the plasma membrane. However, in modelling the electro-permeabilization process, several physical constants need to be approximated in order to obtain realistic results from the numerical scheme approximating the theoretical model (circuital or field based).

In this work we have developed an electric model for living cells in order to predict an increasing probability for electric field interactions with intracellular substructures of cells when the electric pulse duration is reduced to the nanosecond range. Our model consist of a modified Hodgkin-HuxleyCtype non linear equivalent circuit for the outer cell membrane, pore formation and the effect of pores on the conductivity of the outer cellular membrane are taken into consideration. Moreover, the accumulation or depletion of ions in a restricted space surrounding the outer cell membrane (variable concentration), coupled with a linear R_C equivalent circuit for the nuclear membrane is considered.

The pore formation is governed by the so called Smoluchowski equation, which determines, together with the modified nonlinear equivalent circuit, a non linear behaviour of the conductivity of the outer cell membrane with the applied field. In order to take into account the parameters variations and/or uncertainties, in value or dislocation inside the system, an accurate range analysis is carried out. This approach, representing a peculiar aspect of this work, gives the possibility of evaluating the range of electrical pulses values (amplitude, rise time, duration) to be applied, in order to obtain reversible or irreversible effects on the cellular membrane.

A Novel Multiband and Broadband Fractal Patch Antenna

J. J. Huang, F. Q. Shan, and J. Z. She
Tsinghua University, China

Abstract—a novel multiband and broadband fractal patch antenna is presented in this paper. The proposed antenna is compact, simple to design and fabricate. The impedance bandwidth of the proposed antenna could reach 18%, which has rarely been reported for single layer and single patch antennas. Multiband characteristics are also observed and analyzed. All results are proved by simulation and experiment.

1. Introduction

Microstrip patch antenna (MPA) has attracted wide interest due to its important characteristics, such as light weight, low profile and low cost, mechanically robust, simple to manufacture, easy to be integrated with RF devices, allow multi-frequency operation to be achieved, etc. However, its further use in specific systems is limited because of its relatively narrow bandwidth. The impedance bandwidth of a typical patch antenna may be just 1–2%. Much intensive researches have been done in recent years to develop bandwidth-enhancement techniques: using a thick air or foam substrate results in a maximum bandwidth of less than 10%; using stacked or co-planar parasitic patches [1] obtains a bandwidth of 10%–20%; using a gap-coupled probe feed [2] achieves a bandwidth of 16%; more recently, the addition of a U-shaped slot [3] and the use of an L-shaped probe have both been shown to provide bandwidth in excess of 30%. However, these techniques increase antenna volume, complicate the design and fabrication of the antennas.

Fractal geometries have recently been introduced in the design of antennas. It has been shown that fractal shaped antennas exhibit characteristics that are associated with the geometric properties of fractals. One property associated with fractal geometry that is used in the design of antennas is self-similarity. A fractal antenna can be designed to receive and transmit over a wide range of frequencies using the self- similarity properties associated with fractal geometry structures.

In this paper, a novel multi-band and broadband fractal patch antenna is designed, measured and analyzed. The impedance Antenna Structure bandwidth of the proposed antenna could reach 18%, which has rarely been reported for single-layer and single-patch antennas. As the scale Ra increases, multi-band characteristics are observed. All results are validated by simulations and experiments.

2. Antenna Structure

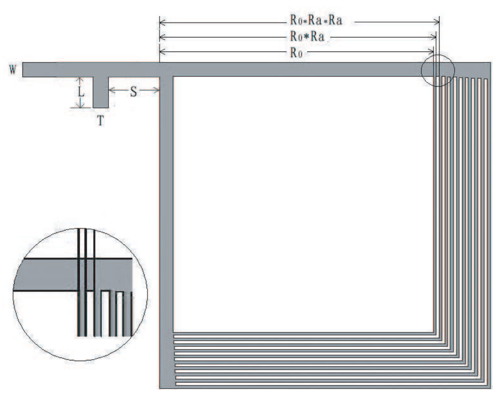

Figure 1: Geometry of the broadband and multi-band fractal microstrip antenna with a tuning stub.

Figure 1 shows the geometry of the fabricated antenna. The exact dimensions for the proposed antenna are also given in Figure 1. The patch is printed on a microwave substrate FR4 of the thickness $H = 1\,\mathrm{mm}$ and the relative permittivity $\varepsilon_r = 4.4$. The antenna is fed through a 50 ohm microstrip line of the width $W = 2\,\mathrm{mm}$. As the FR4 substrate is not suitable to be used at frequencies above 4 GHz, $R0$ should not be too small. For the present design $R0 = 40\,\mathrm{mm}$. The radiation elements are composed of ten similar orthogonal bars. Both the length and width of the orthogonal bar are magnified by the factor of $Ra * Ra$. Four antennas with different

Ra (1.01, 1.02, 1.03 and 1.05) are simulated, fabricated and measured. A tuning stub with the width T and the length L is added to the feed-line of the antenna of $Ra = 1.01$ to get a wider bandwidth of 18%.

3. Simulated and Measured Results

The proposed antenna is simulated using Ansoft HFSS 9.2 and measured with a HP8510C network analyzer. Figure 2 compares the simulated and measured return loss of the antenna of Ra=1.01. The measured impedance bandwidth of the un-tuned antenna is approximately 11% (2.996 GHz–3.321 GHz) while that of the tuned antenna is approximately 18% (3.03 GHz–3.65 GHz). In addition, the antenna has a resonant frequency around 0.9 GHz, which proves the electrically small characteristics of the antenna. Good agreement can be seen between the simulated and measured results.

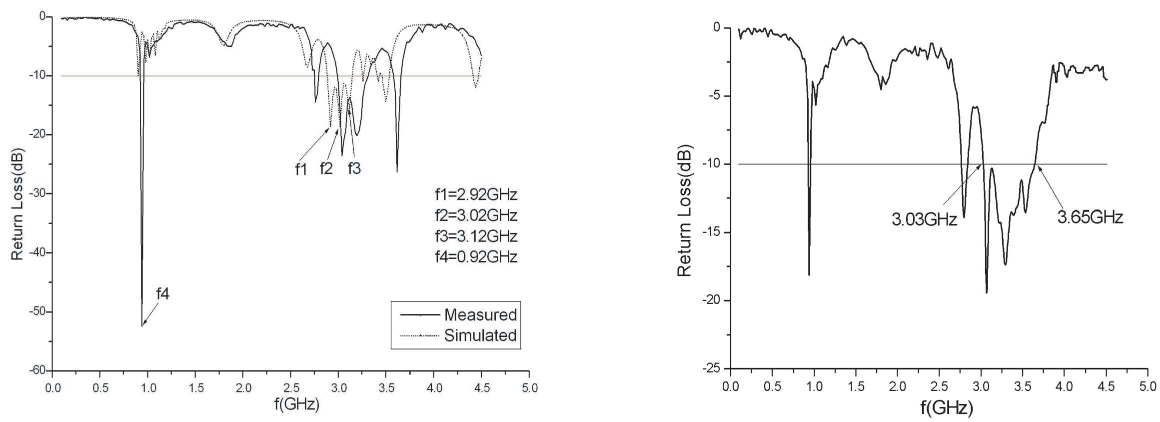

(a) Return loss of the un-tuned antenna ($Ra = 1.01$).

(b) Measured return loss of the proposed antenna ($Ra = 1.01$, $S = 3$ mm, $T = 2.5$ mm, $L = 4$ mm).

Figure 2: Return loss of tuned and untuned antenna.

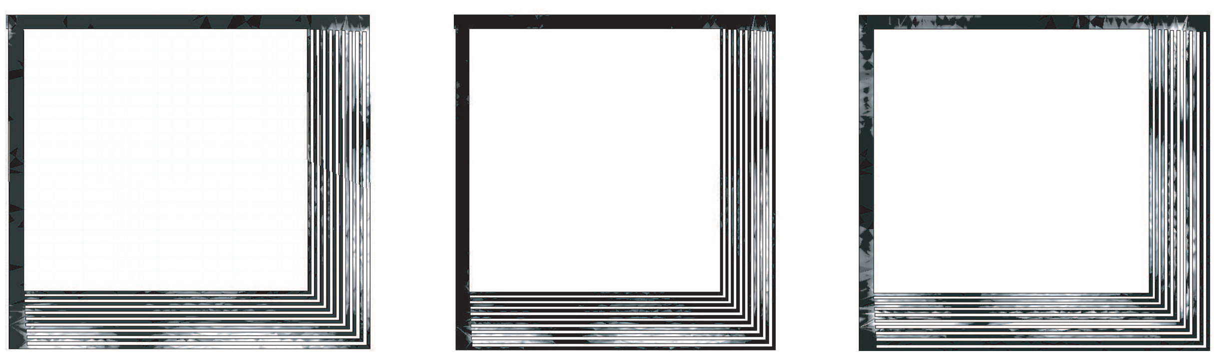

(a) f1=2.92 GHz (b) f2=3.02 GHz (c) f3=3.12 GHz

Figure 3: Surface current distribution at f1, f2 and f3.

From Figure 2(a), one can see that three frequencies f1, f2 and f3 which are close to each other result in a wide bandwidth. Figure 3 shows the simulated surface current density of the three frequencies. When working frequency increases, the area surface current mainly distributed on moves from outer bars to inner bars. Because the dimension of the bars vary slowly by the factor of $Ra * Ra = 1.02$, the antenna has several resonant frequencies close enough to each other to form a wide bandwidth. One can see that f1, f2 and f3 increase by the factor of 1.03, which agrees with the geometry of the structure.

Four antennas of $Ra = 1.01$, 1.02, 1.03 and 1.05 are fabricated and measured to study the influence of the parameter Ra on the antenna's characteristics. Figure 4 shows each return loss of the antennas. Figure 4 also shows that when Ra increases, the antenna change from a broadband antenna ($Ra = 1.01$ and 1.02) into a multi-band antenna ($Ra = 1.03$ and 1.05). As Ra becomes larger, the dimensions of the bars and the working region vary faster, the resonant frequencies is not close enough to each other to form a wide bandwidth.

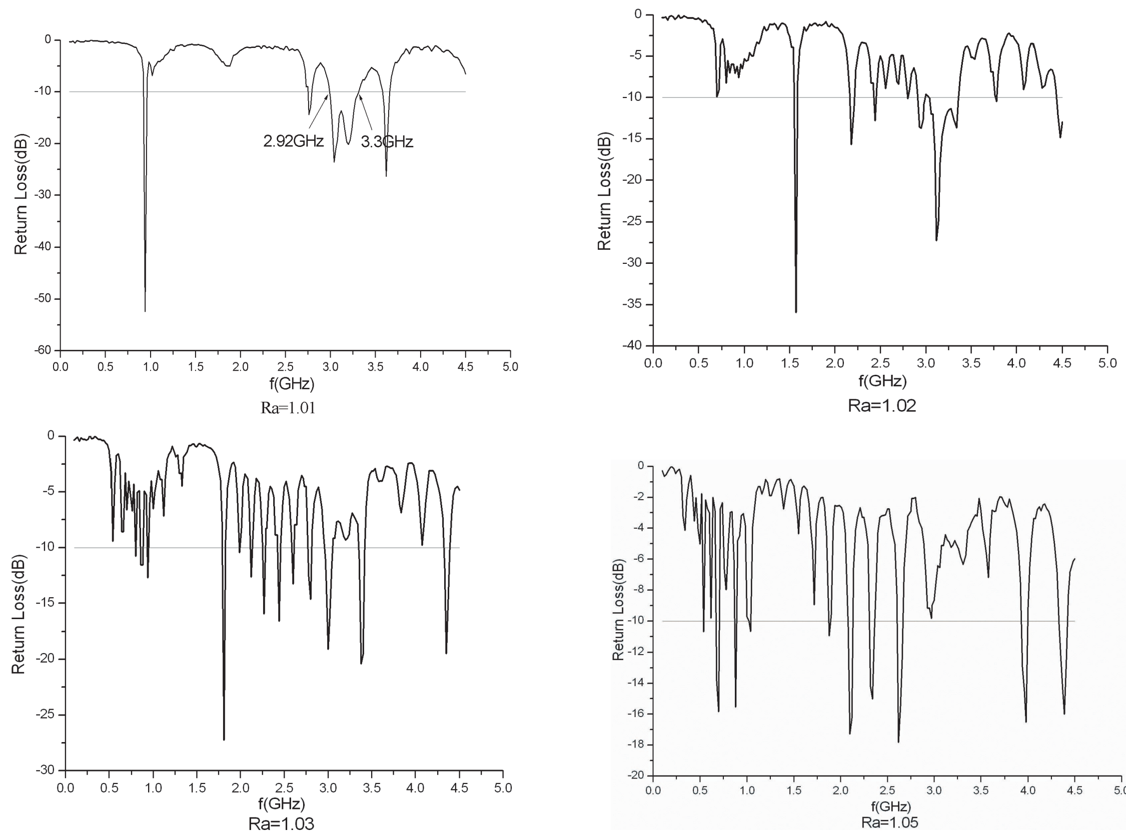

Figure 4: Return loss of four antennas with different Ra.

The radiation characteristics are also studied. Typical results of the tuned antenna at 3.30 GHz are shown in Figure 5.

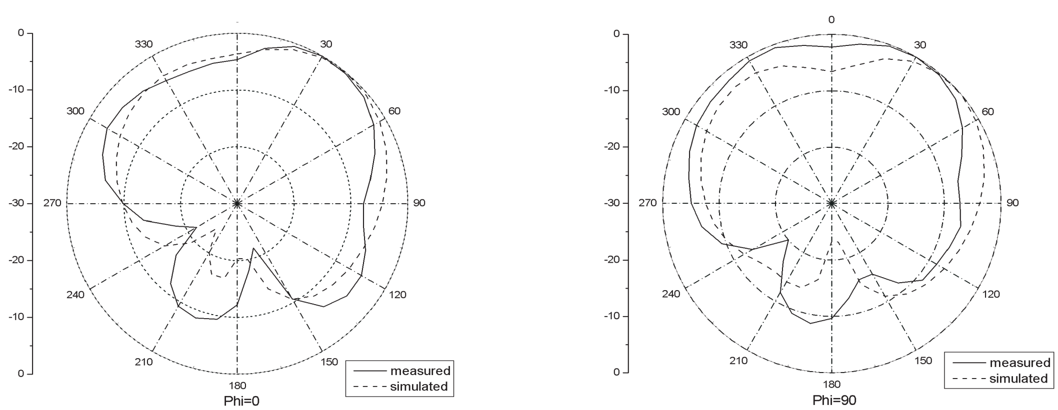

Figure 5: Radiation pattern at 3.3 GHz of the tuned antenna.

4. Conclusion

A novel fractal microstrip antenna with multi-band and broadband characteristics has been successfully demonstrated. The obtained impedance bandwidth of the antenna ($Ra = 1.01$) can be 18% around 3.3 GHz. As Ra increases, Multi-band characteristics of the proposed antennas are also observed. The antenna is compact, simple to design and easy to fabricate.

REFERENCES

1. Lee, R. Q., K. F. Lee, and J. Bobinchak, "Characteristics of a two-Layer electromagnetically coupled rectangular patch antenna," *Electron. Lett.*, Vol. 23, 1070–1072, 1987.
2. Hall, P. S., "Probe compensation in thick microstrip patches," *Electron. Lett.*, Vol. 23, 606–607, 1987.
3. Bhalla, R. and L. Shafai, "Resonance behavior of single u-slot microstrip patch antenna," *Microwave Opt. Technol. Lett.*, Vol. 32, No. 5, 333–335, 2002.
4. Mak, C. L., K. M. Luk, K. F. Lee, and Y. L. Chow, "Experimental study of a microstrip patch antenna with an l-shaped probe," *IEEE Transactions on Antennas and Propagation*, AP-48, 777–782, 2000.

Improvement of Reflectarray Performances at Millimeter Waves by Reduction of the Cell Size

J. Lanteri, C. Migliaccio, J. Y. Dauvignac, and C. Pichot
Université de Nice Sophia-antipolis, France

Abstract—In this paper we discuss the advantages and limitations of reducing the cell size of reflectarrays elements. Reflectarrays have demonstrated their utility at mm-Wave because of their compactness, flexibility and quasi-optical feed that reduces losses. Several applications have been covered such as the automotive cruise control including beam scanning. Most of them use $\lambda/2$ cell sizes. We have investigated and compared performances of reflectarrays with 15 mm and 50 mm diameters using $\lambda/2$ and $\lambda/4$ cell sizes at 94 GHz. Measurements on reduced cell size reflectarrays have demonstrated a loss of 1 dB over 60° beam scanning whereas it is of 3 dB for the $\lambda/2$ structure in the case of the smaller reflector. Nevertheless, this effect is not demonstrated on the largest one because of the phase compensation range that is limited by the variation in the patch dimensions. The maximum corrected phase values are of 320° and 240° for $\lambda/2$ and $\lambda/4$ cells respectively. Furthermore a program based on the ray tracing theory has been developed in order to evaluate the influence of the cell size on the array performances.

1. Introduction

Reflectarrays consist of printed elements, typically patches or dipoles representing the elementary cell of the array. They are designed to scatter the incident field, coming from a feeding antenna, with the proper phase required to form a planar phase surface. They have been developed in the millimeter-wave domain since over 10 years [1] in regards to their low profile and low cost. Most of the classical array characteristics have been studied in order to obtain beam scanning [2], or high aperture efficiency both for linear or circular polarization [3]. Efforts have been made for finding appropriated patch shapes for increasing the variation of the reflected phase, the bandwidth or the fabrication simplicity [4, 5].

In this paper, we investigate the influence of the cell size on the gain and beam scanning performances. The elementary cell consists in a rectangular patch printed on a thin substrate. As the patch shape is not the aim of this work, it has been chosen in order to be simple to design regarding to the cell size variation. The first section describes the measured performances of two small reflectarrays with cell sizes of $\lambda/2$ and $\lambda/4$ respectively, at the operating frequency of 94 GHz. In the second section, a program based on the ray tracing theory is presented and tested on different structures in order to demonstrate the effects of the cell size reduction. Finally limitations are discussed.

2. Influence of the Cell Reduction on a 15 mm Diameter Reflectarray

Two reflectarrays of 15 mm diameter were designed and measured at 94 GHz. They are chosen to be small (about 5λ) in order to avoid the effect of the phase compensation limitation. Indeed, when frequency increases, it becomes difficult to cover 360° of reflection phase with a square patch since its dimensions become too small to be fabricated by classical printed circuit techniques. One solution could be to use sophisticated lithography, like the one based on glass mask. It drastically increases the fabrication cost, thus decreases the competitivity of reflectarrays toward other high gain antenna systems such as dielectric lenses or parabolic reflectors.

The primary source is a standard WR-10 open waveguide that radiates a power pattern that can be approximated by $\cos^5(\theta)$. Considering the spillover and taper efficiencies relations given in [1], a diameter to focal length ratio of 2 provides spillover and taper efficiencies of 87 and 89% respectively. Thus focal length is chosen to be of 7.5 mm. Figure 1(a) and (b) show the upper side of the two reflectarrays. Patch size is optimised by numerical simulations provided by the commercial three-dimensional finite element method solver (HFSS) using the periodic structure module. The substrate is Duroid of dielectric constant 2.2 and 0.381 mm thickness. Phase range compensations are of 320° for the $\lambda/2$ cell and 240° for the $\lambda/4$ one. Nevertheless, due to the small size of the reflector, the number of rings with missing phase values is only of one. Thus their effect is decreased.

Reflectarrays are measured at 94 GHz for a scan angle up to 60° as described in Figure 2. Results are reported in Figure 3(a) and 3(b). A reflectarray with $\lambda/2$ cells performs a loss of gain of 3 dB while scan angle moves. The $\lambda/4$ cells exhibit only 1 dB loss. These results are expected due to the increase of phase accuracy. Additionally, an increase of 2.3 dB is observed on the gain when the cell size is $\lambda/4$.

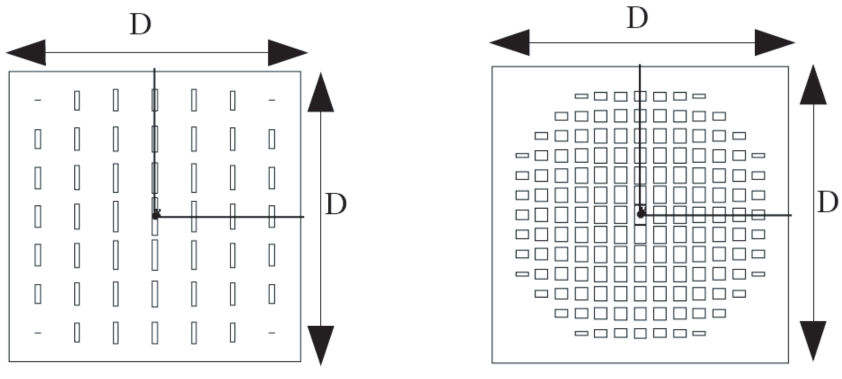

Figure 1: (a)($\lambda/2$) cell, (b)($\lambda/4$) cell.

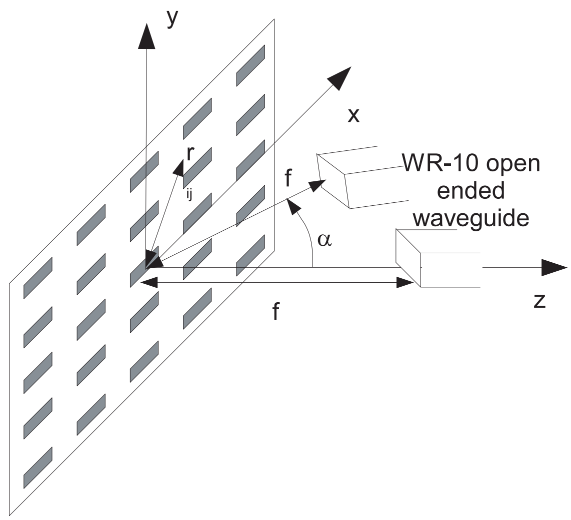

Figure 2: Measurement setup.

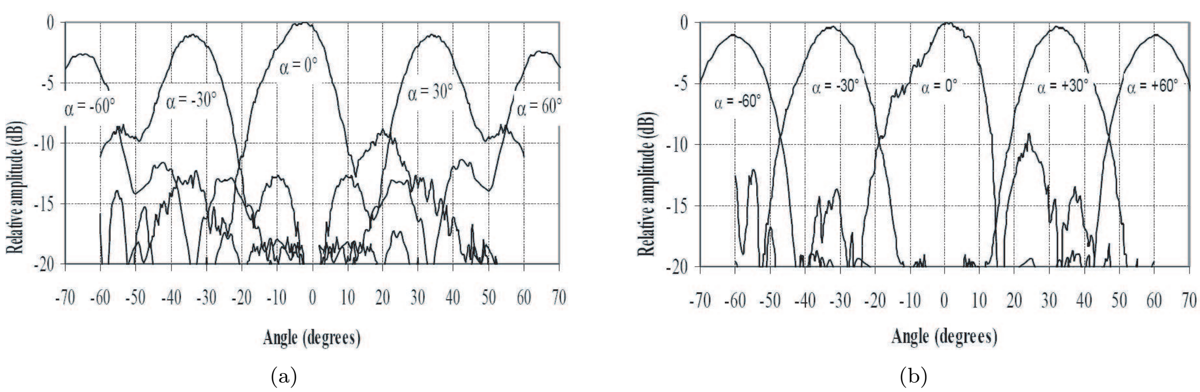

Figure 3: (a)$D = 1(\lambda/2)$ cell size, (b)($\lambda/4$) cell size.

3. Analysis Program

A program based on ray tracing theory was developed in order to investigate the influence on the cell size reduction. It was implemented using Scilab [6]. The surface of the reflectarray is divided into square cells of $\lambda/2$ or $\lambda/4$ size depending on the structure under study. Values of the desired compensation phases are calculated taking into account the directions of incident spherical and reflected plane wave, including offset feeds and scan angles as described in [1]. A complex amplitude coefficient is affected to each cell. Its module is the value of the power pattern described before. The phase is the difference between the formerly calculated one and the compensated one computed by simulations. If the 360° phase could be covered by the square patch, this difference should be of zero in the desired maximum radiation direction. A matrix of complex coefficient is generated. If we denote θ the angle with respect to the z axis described in Figure 2, power density along θ is calculated by making the sum of all the coefficients of the complex matrix for each angle θ. The advantage of using a software as scilab is the possibility to create 3D matrix whose two first dimensions represent the physically 2D reflector and the third one represents the scan angle θ. As a consequence, the time of calculation is reduced. Radiated power is calculated over the power density integration assuming that the radiation pattern is the same over the φ angle. This does not take into account the real primary source radiation pattern such as the square shape of the reflectarray. Radiation pattern is finally plotted after the normalization of the power density by the radiated power. Figure 4 shows the results for the 15 mm reflector. It is obvious that the effect on the beam scanning improvement is the same as the measured one. Gain values are much higher in the simulation. It can be explained by several factors: the simulation does not take into account the primary source blockage, neither the coupling between primary the source and the reflectarray which are both critical in regard to the very short focal length.

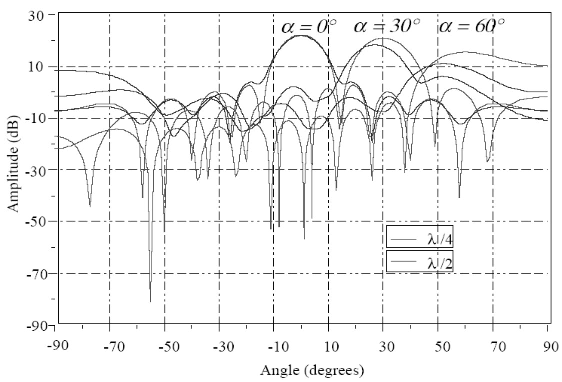

Figure 4: Simulated radiation pattern of the 15 mm reflectarray with different cell sizes.

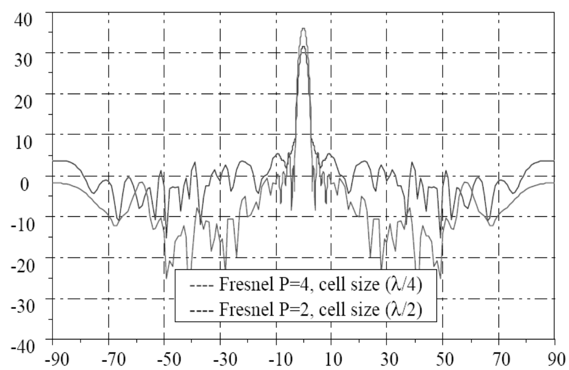

Figure 5: Simulated radiation pattern of Fresnel reflectors with $D = 100$ mm.

The same program is tested on reflector using Fresnel zones phase compensation, whose formula is reminded bellow:

$$R_n = \sqrt{\left(2n\frac{\lambda}{P}\right) + \left(n\frac{\lambda}{P}\right)^2}$$

where R_n is the radius of the Fresnel zone referred to the reflector center, λ the free space wavelength, f the focal length and P the Fresnel correction factor (for example $P = 2$ for a half-wavelength Fresnel reflector). In this case, the effect of the cell size reduction can be seen with different approaches.

First, we consider the effect on size reduction with the same Fresnel correction factor. The improvement of maximal gain is of about 1 dB for a 100 mm diameter half-wavelength reflector.

Second, the space dedicated to each Fresnel zone, defined by $(R_{n+1} - R_n)$ decreases when n increases. As a consequence, high values of P cannot be obtained because the cell size becomes larger than the space for the zone. It can be overcome by using a reduced cell size. The same reflector as described above can be simulated with $P = 4$ if $\lambda/4$ cell size is used whereas cell size of $\lambda/2$ limits P to 2. Results are plotted in Figure 5. The gain increases of 4.4 dB which corresponds to a 50% improvement due to the passage from half- to quarter-wavelength Fresnel reflector enhanced by the cell reduction.

4. Limitations

Larger reflectors of 50 mm diameter have been made and tested without performing the formerly described ameliorations. Considering the limit values of the corrected angles, which are of 320° for the $\lambda/2$ cell and 240° for the $\lambda/4$ one, the program has been modified including this limitation. The number of uncorrected rings increases in comparison to the smaller reflector as shown in Figure 6. Results are plotted in Figure 7. It is obvious that the formerly improvements disappear when the phase compensation range of 360° is not covered.

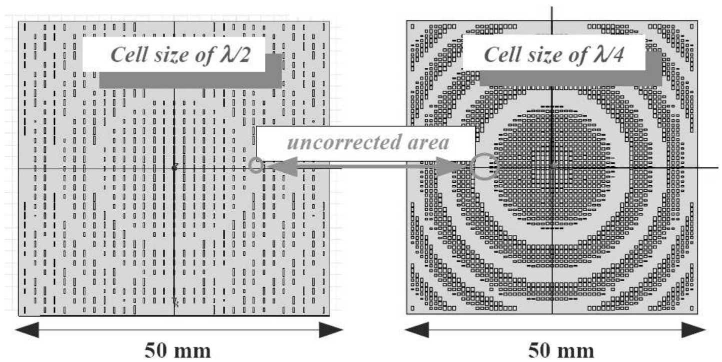

Figure 6: 50 mm diameter reflectors with uncorrected zones.

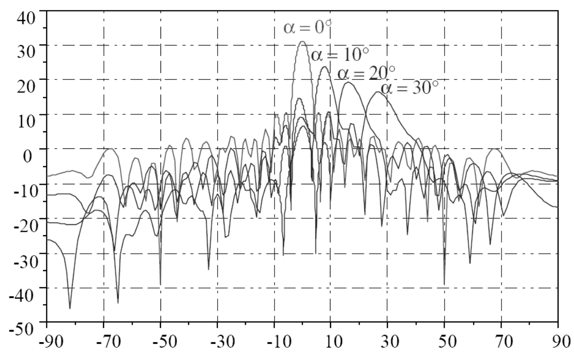

Figure 7: Simulated radiation pattern showing the limitation of cell sizes reduction.

5. Conclusion

We have shown that the cell reduction of reflectarrays provide a gain enhancement and better beam scanning for classical reflectarrays. In case of Fresnel reflectors, the increase of the gain is more important since the cell size reduction enables to increase the Fresnel correction factor P. Nevertheless, making reflectors with cell of $(\lambda/4)$ encounters the difficulty to obtain a phase reflection compensation of 360°, specially at mm-Wave. In this case, performances are strongly decreased. New patch shapes have to be investigated in order to overcome this problem.

REFERENCES

1. Pozar, D. M., S. D. Targonski, and H. D. Syrigos, "Design of millimeter wave microstrip reflectarrays," *IEEE Trans. Antennas Propagat.*, Vol. 45, No. 2, 287–296, February 1997.
2. Menzel, W., D. Piz, and M. Al-Tikriti, "Millimeter wave folded reflector antennas with hign gain, low loss, and low profile," *IEEE Antennas and Propagation Magazine*, Vol. 44, 24–29, June 2002.
3. Huang, J. and J. Pogorzelski, "A ka-band microstrip reflectarray with elements having variable rotation angles," *IEEE Trans. Antennas Propagat.*, Vol. 46, 650–656, May 1998.
4. Misran, N., R. Cahill, and V. F. Fusco, "Design optimisation of ring elements for broadband reflectarray antenna," *IEE Proc.-Microw. Antennas Propag.*, Vol. 150, No. 6, 440–444, December 2003.
5. Nguyen, B. D., C. Migliaccio, and C. Pichot, "94 GHz Zonal ring reflector for helicopter collision avoidance," *Electronics Lett.*, Vol. 40, No. 20, 1241–1242, 2004.
6. Scilab 3.0 (ENPC, INRIA): www.scilab.org .

Optical Near-field Study of Dielectric Nanostructures

M. Y. Mahmoud[1], G. Bassou[1,2], L. Salomon[2], Z. Chekroun[1], and N. A. Djamai[1]

[1]Université Djilali Liabès de Sidi Bel-Abbes, Algérie
[2]Université de Bourgogne, France

The photon scanning tunneling microscope is based on the frustration of a total internal reflection beam by the end of an optical fiber. This microscope has been used to obtain topographic information generally on smooth samples. We study the influence on image formation of several parameters in scanning near-field microscopy. The numerical calculations have been carried out using the differential method. We consider the case of three-dimensional system including a translational symmetry in one direction. Various oscillations patterns are observed from both sides of the nanostructure, which we interpret as interference between the diffracted waves scattered by the nanostructure (with the components of the wave vector parallel to the surface) and the evanescent incident wave above the surface. The period of oscillations depends on several parameters. The numerically obtained period corresponds well to the expected theoretical value. Using an optical near-field analysis and by calculating the electric field intensity distribution, we investigate the probe-sample distance effect. It is found that the distribution of the intensity related to the electric field is depending on sample-probe distance. We noticed the loss of details in the image and the presence of strong oscillations. Also, both of the polarization state of the illuminating light effect and the angle of incidence are investigated. We show how the depth of penetration has an effect on the field intensity distribution. After that we pay more attention to the depth of penetration. The analytical values of the penetration depth of the incident electromagnetic field of the system are in good agreement with the numerical values obtained with a differential method. We conclude that a differential method provides physical insight into the main features of the different images.

Array Patterns Synthesizing Using Genetic Algorithm

J. Jin, **H. L. Wang**, **W. M. Zhu**, **and Y. Z. Liu**
Nanjing Institute of Communications Engineering, China

Abstract—A planar array antenna with arbitrary geometry synthesis technique based on genetic algorithm is discussed. This approach avoids coding/decoding and directly works with complex numbers to simplify computing programming and to speed up computation. This approach uses two crossover operators that can overcome premature convergence and the dependence of convergence on initial population. Simulation results show that this method is capable of synthesizing arrays whose elements are located on irregular grids, and generates quite complex shapes and can realize good sidelobe suppression at the same time.

1. Introduction

In the interests of efficiency, the shape of a footprint pattern radiated by a satellite-borne array antenna should conform precisely to the shape of the region on Earth for which coverage is required. Alternatively, in order to achieve "isoflux" illumination [1] on the earth surface through multi-beams, the size and the shape of the footprint should be precisely controlled.

Previous works on the synthesis of arrays for arbitrary footprint shapes include Chebyshev method, modified Woodward–Lawson method and a series of methods based on sampling a circular Taylor distribution [2–4]. But these methods have the drawback that they require the arrays to lie on a rectangular lattice or circular lattice. Some methods require the aperture of the array to be regular shape.

Genetic algorithm (GA) has a high ability in global optimization. It is an increasingly popular optimization method being applied to many fields of endeavor, including electromagnetic optimization problems.

Use genetic algorithm to synthesize array pattern has no limitation on lattice shapes and aperture shapes. It can synthesize planar array with arbitrary geometry and generating arbitrary patterns. Conventional GAs [5, 6] with binary coding and binary genetic operation are inefficient and inconvenient for array pattern synthesis problems to optimize complex numbers. Unlike conventional GAs, this approach avoids coding/decoding and directly deals with complex excitation vectors.

Compared with other numerical methods [7, 8], this approach has unique features to treat complicated problems (complicated arrays and complicated pattern shapes).

2. Problem Formulation

The far-field radiation pattern $F(\theta, \varphi)$ at a far-field angle (θ, φ) from array broadside is given by

$$F(\theta, \varphi) = EF(\theta) \cdot AF(\theta, \varphi) \tag{1}$$

where

$$EF(\theta) = \cos^{1.5}(\theta) \tag{2}$$

is the element radiation pattern; $AF(\theta, \varphi)$ is the array factor. For an arbitrary array, the Array Factor (AF) can be expressed by the general function:

$$AF(\theta, \varphi) = \mathbf{I}\mathbf{s}(\theta, \varphi) \tag{3}$$

$$\begin{aligned}
&\mathbf{I} = [I_1, I_2, ..., I_N], I_n \in C^n,\\
&\mathbf{s} = [e^{jkr_1\hat{a}(\theta,\varphi)}, e^{jkr_2\hat{a}(\theta,\varphi)}, ..., e^{jkr_N\hat{a}(\theta,\varphi)}]^T,\\
&\mathbf{r}_n = \hat{\mathbf{a}}_\mathbf{x} x_n + \hat{\mathbf{a}}_\mathbf{y} y_n + \hat{\mathbf{a}}_\mathbf{z} z_n,\\
&\hat{\mathbf{a}}(\theta, \varphi) = \hat{\mathbf{a}}_\mathbf{x} \sin\theta\cos\varphi + \hat{\mathbf{a}}_\mathbf{y} \sin\theta\sin\varphi + \hat{\mathbf{a}}_\mathbf{z} \cos\theta
\end{aligned}$$

where, $\mathbf{I}$ is the excitation vector, $\mathbf{s}$ is the steering vector, C^n is the set or subset of all complex numbers, $\mathbf{r}_n$ is the element location vectors, $\hat{\mathbf{a}}(\theta, \varphi)$ is unit vector of distance ray of spheric coordinate, and θ and φ are the elevation and azimuth angles respectively. GA is applied to find proper excitation coefficient vector $\mathbf{I}$ to achieve desired pattern shape, sidelobe suppression and steering.

3. The Genetic Algorithm

The GA process could be simplified as following: 1) Initialize a random pool of Individuals. 2) Evaluate each Individual. 3) Choose couples (Mating). 4) Breed them together (Crossover). 5) Evaluate each Individual. 6) Selection. 7) Mutation. 8) If the pool has converged, or a number of pre-determined cycles have been completed, finish the cycle. If not, return to step #3.

A. Construction of Chromosomes

In this approach, chromosomes are represented directly by complex excitation vectors $\mathbf{I}$. N elements complex excitation coefficients are genes of the chromosome.

B. Fitness Function

Evaluation plays a very important role in the GA process. Fitness function maps all the properties of an individual to a floating-point number, essentially, giving it a rank and a place amongst the other individuals in the pool. Creating the fitness function is one of the most difficult works in the creation of a GA solution.

In this approach, we desired that the magnitude $|F(\theta,\varphi)|$ of the far-field pattern remain bounded between some specified limits as

$$\left|F_{\text{min limit}}(\theta,\varphi)\right| \le |F(\theta,\varphi)| \le \left|F_{\text{max limit}}(\theta,\varphi)\right| \tag{4}$$

A cost measure to be minimized is the sum of the squares of the excess far field magnitude outside the specified bounds. This can be written as

$$\begin{aligned} f_1 \;=\;& c_1\sum_{j=1}^{J}\sum_{k=1}^{K}\max(|F(\theta_j,\varphi_k)| - \left|F_{\text{max limit}}(\theta_j,\varphi_k)\right|,0)^2 \\ &+c_2\sum_{j=1}^{J}\sum_{k=1}^{K}\max(\left|F_{\text{min limit}}(\theta_j,\varphi_k)\right| - |F(\theta_j,\varphi_k)|,0)^2 \end{aligned} \tag{5}$$

where, $|F(\theta,\varphi)|$ are the far field pattern values from (1) evaluated at $J\times K$ far-field angles (θ_j,φ_k). θ_j and φ_k are spaced in some rules. This will be decided by the beam-pointing angle. c_1, c_2 are weights.

If the dynamic range ratio $|I_{\max}/I_{\min}|$ is too large, the excitation will not easy to realize. We can limit it using the following fitness function:

$$f = f_1 + c_3(|I_{\max}/I_{\min}|) \tag{6}$$

where, c_3 is a weight parameter. Lower values of f indicate better fitness.

C. Mating Scheme

Yeo [9] discussed three mating schemes and thought if one or more near-solutions were added to an initial population of random individuals, EMS scheme usually yields the best chromosome among these three methods. However, this scheme always results in prematurity. In this approach, we make use of a stochastic mating scheme. All individuals have chance to mate and no one can mate two times.

D. Crossover

The crossover operator is the most important operator and it is the operator that combines two individuals to create (a) new individual(s), which will, it is hoped, become better than his/their parents. This might and can work because the selection operator chooses the better individuals.

Real coded GAs usually use interpolate cross operator to breed offspring. Its operating process can be described as follows,

$\mathbf{I^1}$ and $\mathbf{I^2}$ are parents. The chromosomes of them have N genes. The offspring of them can be written as

$$I_i^{1'} = cI_i^1 + (1-c)I_i^2 \tag{7}$$

$$I_i^{2'} = cI_i^2 + (1-c)I_i^1 \tag{8}$$

where, $c\in[0,1]$, $i=1,2,\ldots,N$.

Extrapolate cross operator is another real number cross operator. The offspring genes of $\mathbf{I^1}$ and $\mathbf{I^2}$ can be written as

$$I_i^{1'} = I_i^1 - (I_i^2 - I_i^1)c \tag{9}$$

$$I_i^{2'} = I_i^2 + (I_i^2 - I_i^1)c \tag{10}$$

The two real number operator can work with complex number as well. Interpolate cross operator has advantages of fast convergence. Extrapolate cross operator expand the search space. Combining two operators can overcome premature convergence and the dependence of convergence on initial population.

The range of genes is $|I_i| \leq 1$. If genes generated by crossover are out of the bound, then

$$I_i = I_i / |I_i| \, (i = 1, 2, \ldots, N) \tag{11}$$

E. Selection

The selection operator distinguishes the better individuals from the worse individuals using their fitness. In this approach, both the child and parent populations are ranked together in ascending order. Then, based on the principle of survival of the fittest, those producing superior output survive, while those producing inferior output die off. Please note that the competitors for survival selection include both parents and their children so that the members of next generation may include members of the previous generation. This guarantees that the new generation performs no worse than older ones. In other words, the cost f versus generation curve decreases monotonically. This selection scheme includes optimum maintaining strategy.

F. Mutation

The mutation operator plays a secondary role with respect to crossover operators. It can maintain the diversity of the population. Mutation is a minor change to the genes of an individual, in a hope to find an even better solution, or rather, to expand the search space to a point where normal breeding might not reach. Mutation effectively slows down convergence, but might yield better and closer-to-best individuals. If an individual is "pushed" to a different peak area, a higher one, it might "pull" other individuals with the crossover process to the new peak, thus climbing a better and higher peak, and achieving a better solution. Both the probability and the range of mutation can affect convergence [10].

Nevertheless, mutation is required to prevent an irrecoverable loss of potentially useful information that occasionally reproduction and crossover can cause.

The fitness of mutated individual usually has low value. If put mutation in front of selection. The mutated individuals would die off because of the child and parent competition. In this approach mutation is put after selection.

Assuming P_m is the mutation probability, the mutation is as follows: P real numbers are generated in $[0, 1]$ randomly. Each number corresponds to an individual of the population. Set the number corresponding to current optimum to "1" to avoid being mutated. An individual whose corresponding number less than P_m will be muted use (12).

$$\mathbf{I}' = \mathbf{I} + \mathbf{d} \tag{12}$$

where, $\mathbf{d}$ is a vector dimension same as $\mathbf{I}$.

G. Convergence Observation

For fast convergence, the initial population can include approximate excitations by other techniques (such as Fourier expansion method [11], etc.) We care about not only the shape of main beam, but also the sidelobe level. In order to obtain the required sidelobe level rapidly, we put the optimization result of adjacent beams into initial population which can reduce optimization time largely.

In this approach, two crossover operators are used to generate offspring. Adjusting proportions act on population of two operators, i.e., 40% population use interpolate cross operator to generate offspring and 60% population use extrapolate cross operator to generate offspring, can makes the algorithm has a good performance.

4. Simulation Results

This subsection presents a shaping example based on a Low Earth Orbit (LEO) satellite-born antenna array. As shown in Figure 1, a 61 elements antenna array with hexagonal (or equilateral triangular) grid is used.

In order to achieve "isoflux" illumination on the earth surface, a circularly symmetric cell layout was decided as shown in Figure 2 after calculation. Wedge shaped cells are arranged in rings about nadir. There are 23 beams requiring shape, and 30 dB sidelobe suppression is needed.

Figure 3 is the pattern of beam 1. Gain in main beam edge is higher than that in beam center. This can compensate the path loss due to the slant range differences from satellite to earth. Figures 4, 5 and 6 are the patterns of beam 2, 3 and 8. It is observed that the main lobe satisfy the requirement, and side lobe level suppress reach 30 dB which is outstanding the results of [7, 8].

If the dynamic range ratio $|I_{\max}/I_{\min}|$ is too large, the excitation will not easy to realize. For beam 1 shown as Figure 2, $|I_{\max}/I_{\min}| = 20$. For beams in ring 2 and a sidelobe level of –30dB , an $|I_{\max}/I_{\min}| < 40$ can be reached. For beams in ring 3 and a side lobe level of -30 dB, an $|I_{\max}/I_{\min}| < 50$ can be reached. These excitations are easily to realize.

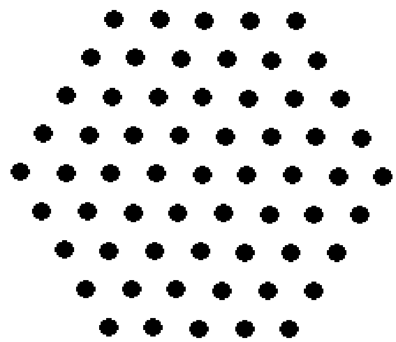

Figure 1: 61 elements antenna array.

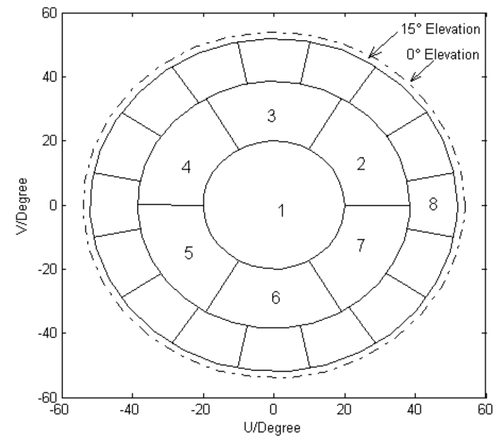

Figure 2: Cells arranged in rings, $U{=}\theta\cos\varphi$, $V{=}\theta\sin\varphi$.

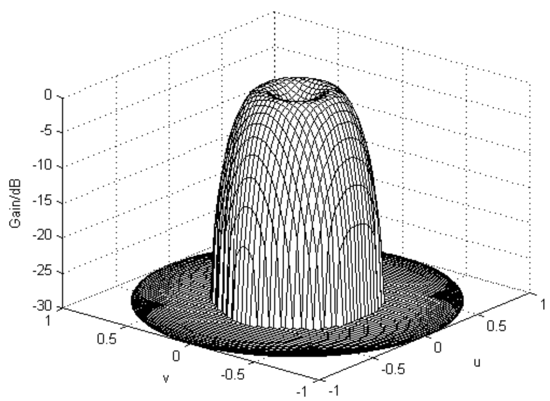

Figure 3: Pattern of beam 1, $u{=}\sin\theta\cos\varphi$, $v{=}\sin\theta\sin\varphi$.

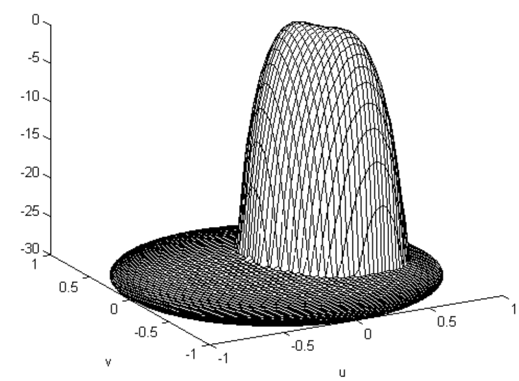

Figure 4: Pattern of beam 2.

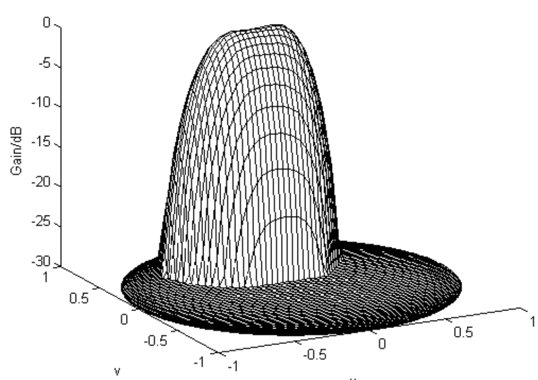

Figure 5: Pattern of beam 3.

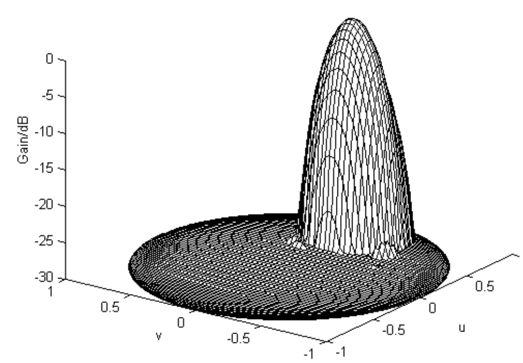

Figure 6: Pattern of beam 8.

If Woodward-Lawson method was used, it requires the elements to lie on a rectangular lattice and require the aperture of the array to be rectangle. And the $|I_{\max}/I_{\min}|$ of the solution will reach 800 or even higher [3].

The -3 dB contour of each beam after being shaped is shown in Figure 7. Notice the shape of beams, for example beams in ring 2, for perfection beamforming the footprints shape should wedge-shaped. Of course, it is achievable only by an infinitely large array. Due to the limitation of aperture size and restriction of elements number, the footprint shapes are kidney-shaped. However, it can satisfy the requirements of isoflux illumination.

Figure 8 shows the gain of beams along U = 0° of the satellite coverage. Path loss due to the slant range differences from satellite to earth is considered. From the slice figure we can see that gain is higher than 13 dBi, and ripples lower than 3 dB.

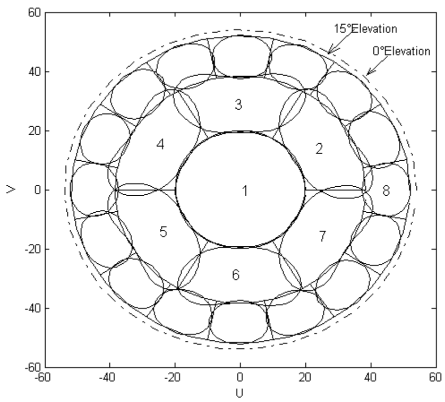

Figure 7: -3 dB contour of each beam.

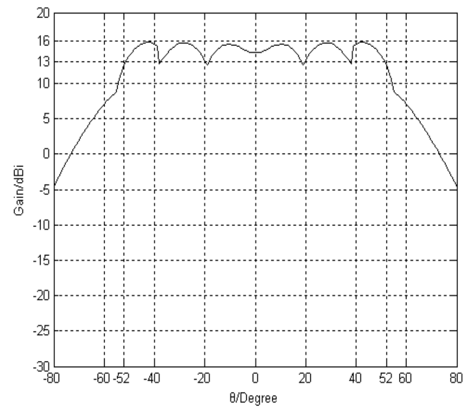

Figure 8: Slice figure of $U = 0°$.

5. Conclusion

A complex coded GA based method is discussed for the synthesis of planar arrays with arbitrary geometry that generate footprints of arbitrary shape. This approach is capable of synthesizing quite complex shapes of 3D patterns for main lobe and can realize good sidelobe suppression at the same time. The method has been proved to be useful for the synthesis of large array antennas whose elements are located on irregular grids.

Acknowledgment

This work was supported by the National Natural Science Foundation of China under Project NSFC60572095.

REFERENCES

1. Sherman, K. N., "Phased array shaped multi-beam optimization for LEO satellite communications using a genetic algorithm[C]," *International Conference on Phased Array Systems and Technology*, Dana Point CA, USA, 21–25, May 2000. 501–504.
2. Wang, M., S. Lv, and R. Liu, *Analysis and synthesis of array antenna*, Chengdu, The ESTC University Press, 1989.
3. Rodríguez, J. A., J. M. Cid, F. Ares, and E. Moreno, "Synthesis of satellite footprints by perturbation of Woodward-Lawson solutions for planar array antennas," *J. Electromagn. Waves Appl.*, Vol. 14, No. 3–10, 2000.
4. Trastoy, A., F. Ares, and E. Moreno, "Arbitrary footprint patterns from planar arrays with complex excitations," *Electron. Lett.*, Vol. 36, No. 20, 1678–1679, 2000.
5. Holland, J. H., "Genetic algorithms," *Scientific American*, Vol. 267, No. 4, 44–50, 1992.
6. Holland, J. H., *Adaptation in natural and artificial systems*, Massachusetts, The MIT Press, 1992.
7. Olen, C. A. and RT. Compton, Jr, "A numerical pattern synthesis algorithm for arrays," *IEEE Trans. Antennas Propagat.*, Vol. 38, No. 10, 1666–1676, 1990.
8. Zhou, P. Y. P. and M. A. Ingram, "Pattern synthesis for arbitray arrays using an adaptive method," *IEEE Trans. Antennas Propagat.*, Vol. 47, No. 5, 862–869, 1999.
9. Yeo, B. K. and Y. Lu, "Array failure correction with a genetic algorithm," *IEEE Trans. Antennas Propagat.*, Vol. 47, No. 5, 823–828, 1999.
10. Boeringer, D. W., D. H. Werner, and D. W. Machuga, "A simultaneous parameter adaptation scheme for genetic algorithms with application to phased array synthesis," *IEEE Trans. Antennas Propagat.*, Vol. 53, No. 1, 356–371, 2005.
11. Rodríguez, J. A., R. Munoz, H. Estévez, and F. Ares, "Synthesis of planar arrays with arbitrary geometry generating arbitrary footprint patterns," *IEEE Trans. Antennas Propagat.*, Vol. 52, No. 9, 2484–2488, 2004.

Space-filling Patch Antennas with CPW Feed

M. R. Haji-Hashemi, **H. Mir-Mohammad Sadeghi**, **and V. M. Moghtadai**
Isfahan University of Technology, Iran

Abstract—In this paper, the performances of some space-filling monopole antennas with coplanar waveguide have been investigated. It may be contended that the bends and corners of these geometries would add to the radiation efficiency of the antenna, thereby improving its gain. Advantage of these configurations is that they lead to multiband conformal antennas. A new version of Gosper curve patch antenna is introduced and its performance has been compared to conventional Gosper curve patch antenna.

1. Introduction

Fractal shaped antennas exhibit some interesting features that stem from their inherent geometrical properties. The self-similarity of certain fractal structures results in a multiband behavior of corresponding fractal antennas and frequency-selective surfaces (FSS) [1, 2].

On the other hand, the high convoluted shape and space-filling properties of certain fractals allow reducing the volume occupied by a resonant element. Theses properties are useful in designing multiband antennas and FSS, and reducing the size of certain antennas.

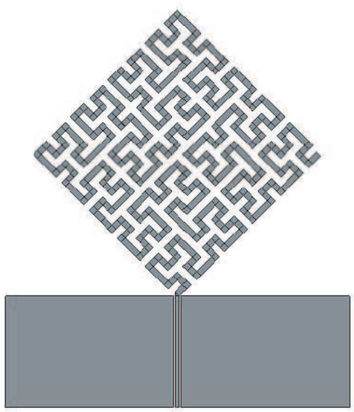

Figure 1: 4^{th} order of Hilbert patch antenna with CPW monopole feed.

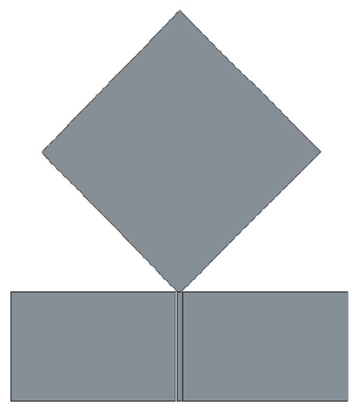

Figure 2: Lozenge shape patch antenna with CPW monopole feed.

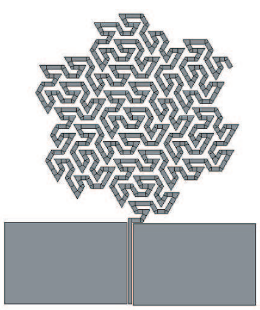

Figure 3: CPW-fed Gosper curve patch antenna.

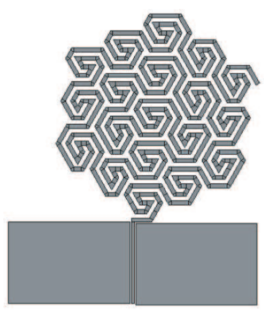

Figure 4: Another version of Gosper curve patch antenna.

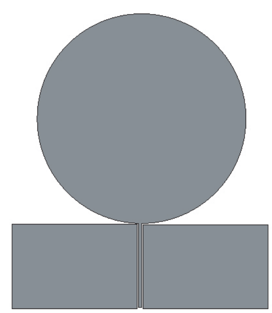

Figure 5: Circular disc CPW-fed monopole antenna.

Microstrip patch Antennas are very popular in many fields as they are low-profile, low weight, robust and cheap. In last years new techniques employing fractal geometries are studied and developed. One of them is the fractalizing of antenna's boundary where new qualitative effect as the higher localized modes appear, that result in directive radiation patterns [3]. Another technique that has been studied in this paper is using space-filling curves as patch radiator.

Space-filling curves map the multi-dimensional space into the one-dimensional space. A space-filling curve acts like a thread that passes through every cell element (or pixel) in the n-dimensional space so that every cell is visited only once. Therefore, the space-filling curve does not self-intersect. Thus, a space-filling curve imposes a linear order of the cells in the n-dimensional space. These geometries have the following properties: Self-Avoidance (as the line segments do not intersect each other), Simplicity (since the curve can be drawn with a single stroke of a pen) and self-similarity [4].

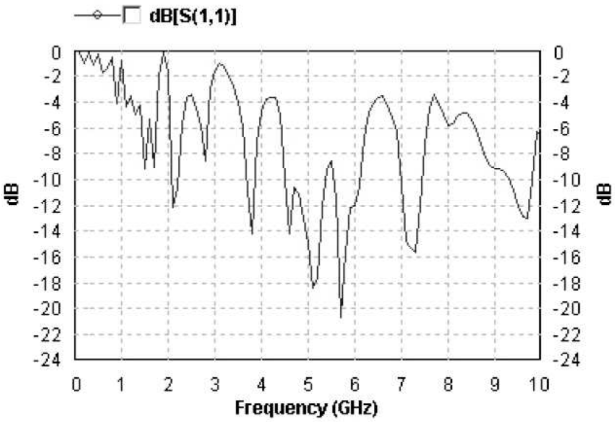

Figure 6: Return loss vs. frequency of antenna configuration in Fig. 1.

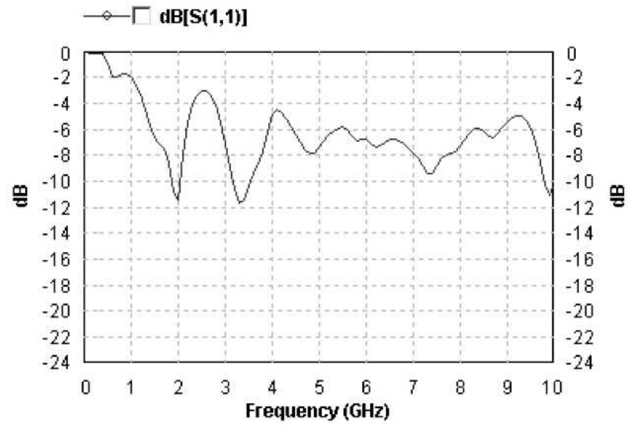

Figure 7: Return loss vs. frequency of antenna configuration in Fig. 2.

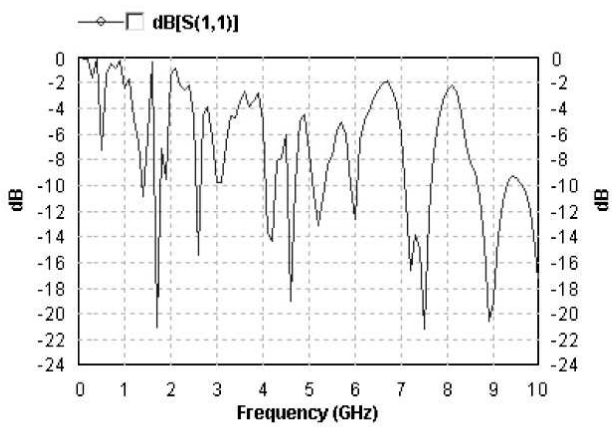

Figure 8: Return loss vs. frequency of antenna configuration in Fig. 3.

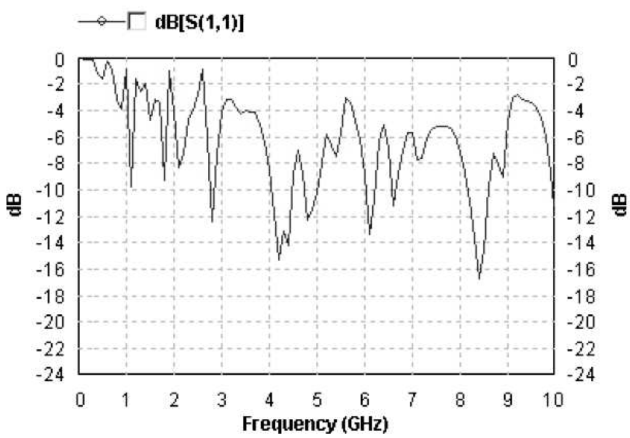

Figure 9: Return loss vs. frequency of antenna configuration in Fig. 4.

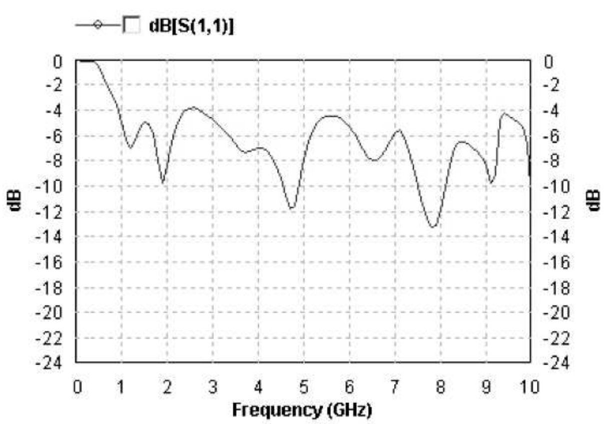

Figure 10: Return loss vs. frequency of antenna configuration in Fig. 5.

There are many types of space-filling curves (SFCs), e. g., the Peano, Hilbert, and Gosper curves, to name a few. They differ from each other in the way they visit and cover the points in space.

In other hand, coplanar waveguide feed is a well-known technique for increasing the bandwidth of patch antennas [5].

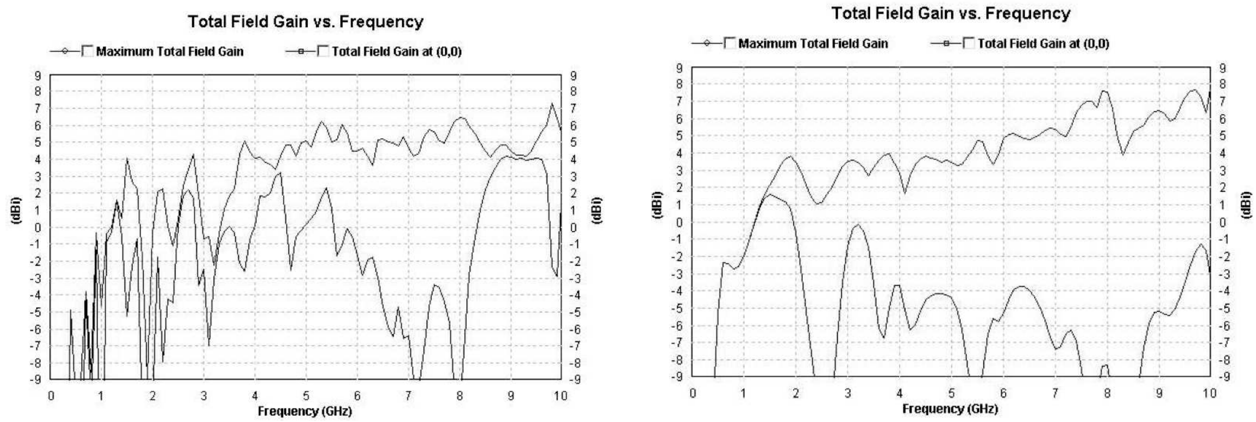

Figure 11: Maximum total field gain and total gain normal to antenna plane vs. frequency of Hilbert curve and lozenge shape antennas (left to right).

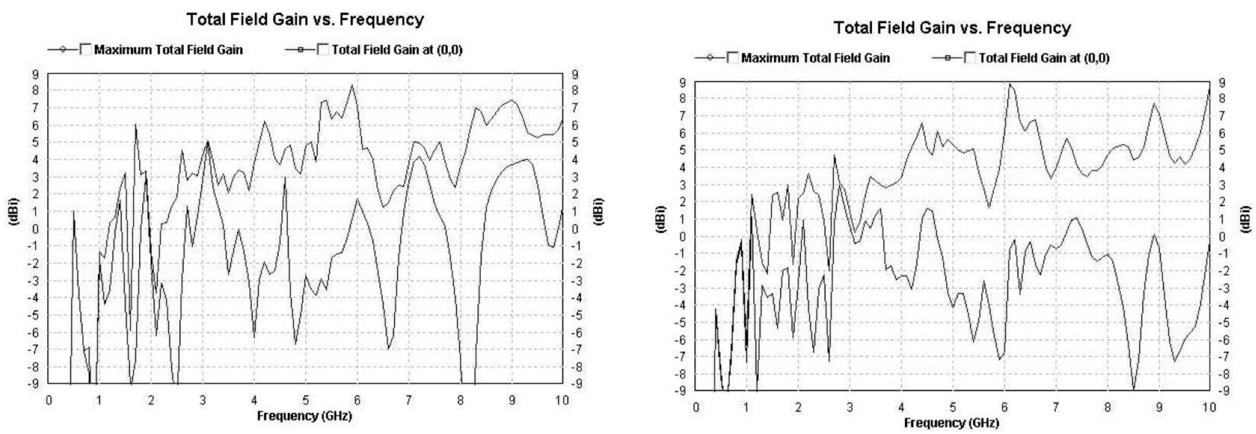

Figure 12: Maximum total field gain and total gain normal to antenna plane vs. frequency of antenna configuration in Fig. 3 and Fig. 4 (left to right).

In this paper, this technique has been imposed on some types of fractal space-filling monopole antennas such as Hilbert curve antenna and Gosper curve antenna.

2. Proposed Antenna Configurations

Schematic of studied structures are shown in Figs. 1–5. These configurations are in a single layer metallic structure. Hilbert curve and Gosper curve radiators are fed through coplanar wave guide monopole feed. For comparison the Euclidean counterparts of these structures have been studied.

Each section of Ground plane has the dimension of 6 cm×4 cm, the width of microstrip feed in every configuration is 1.45 mm while the gap between the strip and coplanar ground plane is 0.1 mm.

The overall height of each space filling curve is assumed to be about 10 cm.

3. Simulation Results

Simulation of the above structures has been done using IE3D MOM-based code. In Figs. 6–10, Return losses versus frequency of these antennas are shown.

Simulation results show that space-filling patch antennas are conformal multiband antennas.

Making a direct relationship between antenna characteristics and geometrical properties of inscribed geometries is not easy. However we can say the results of return loss versus frequency of theses structures show that in same overall dimensions, the space-filling CPW-fed monopole antennas have better performance in input matching characteristics, number of resonant frequencies and bandwidth than their Euclidian counterparts. For instance compare the results of return loss versus frequency of Hilbert curve CPW-fed monopole antenna and lozenge shape CPW-fed monopole antenna (Fig. 6 and Fig. 7) and the results of two versions of Gosper curve CPW-fed monopole antenna and circular disc CPW-fed monopole antenna (Fig. 8 and Fig. 9 with Fig. 10).

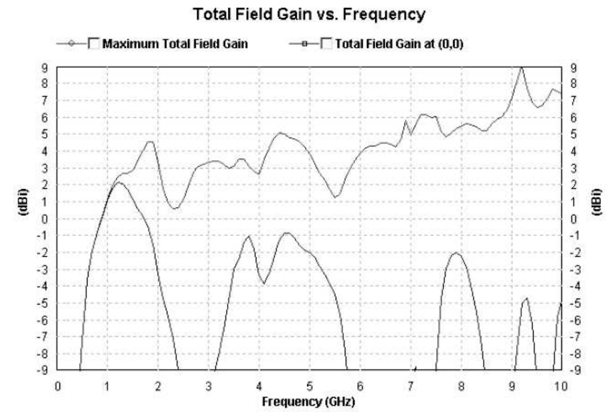

Figure 13: Maximum total field gain and total gain normal to antenna plane vs. frequency of circular monopole antenna (Fig. 5).

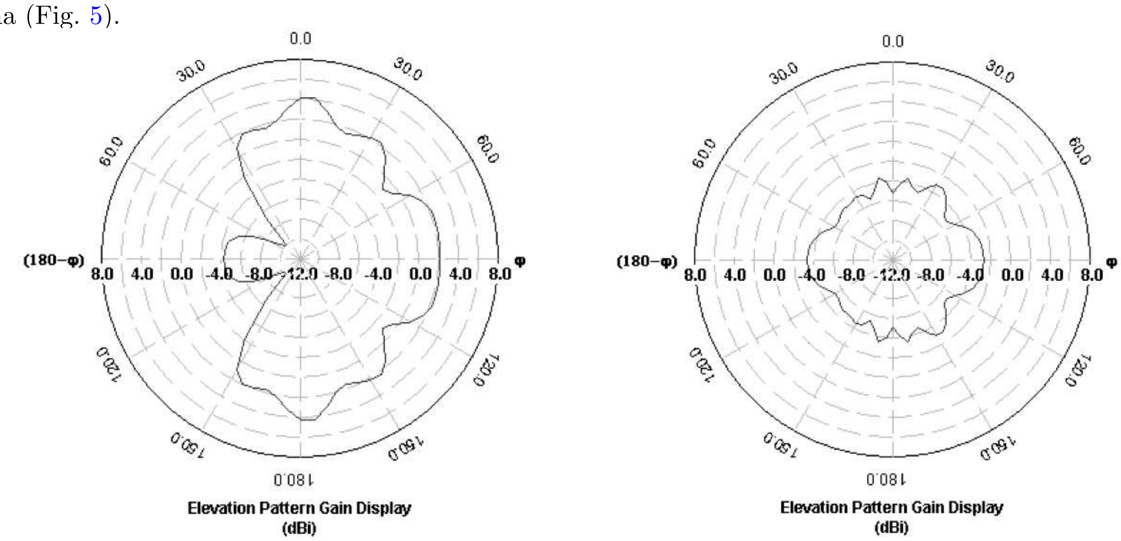

Figure 14: Elevation pattern gain display of Hilbert curve CPW-fed monopole antenna and lozenge shape CPW-fed monopole antenna in 9 GHZ.

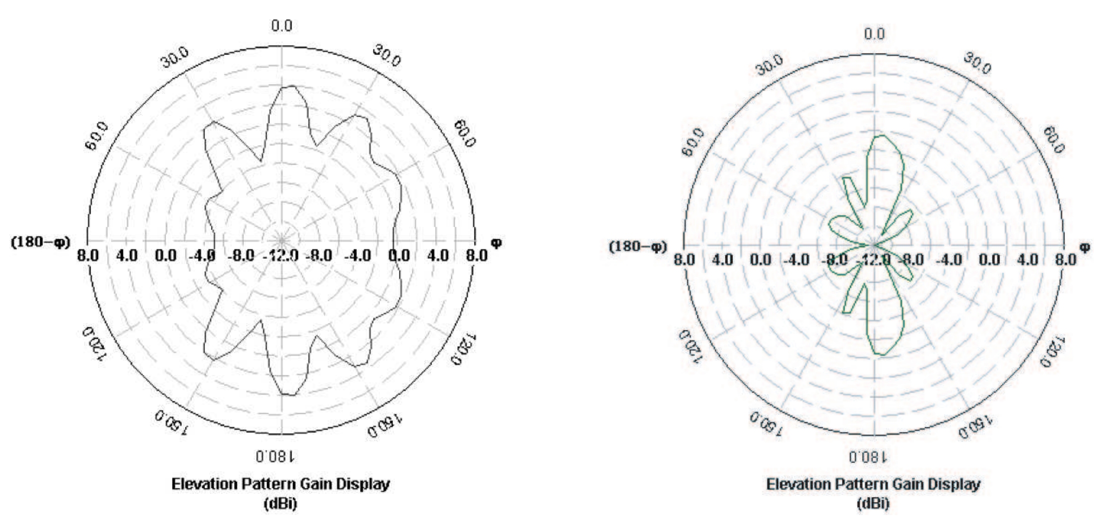

Figure 15: Elevation pattern gain display of two versions of Gosper curve CPW-fed monopole antenna (Fig. 3 and Fig. 4) in 9 GHZ (left to right).

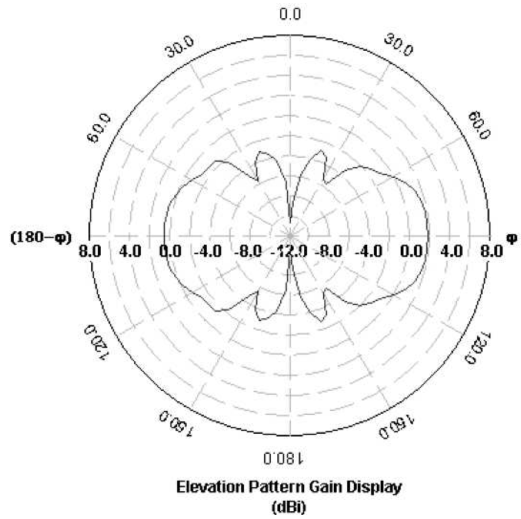

Figure 16: Elevation pattern gain display of circular disc CPW-fed monopole antenna (Fig. 5) in 9 GHz.

Main resonant frequencies of Hilbert curve CPW-fed monopole antenna and lozenge shape CPW-fed monopole antenna are very close together. This can be seen about two version of Gosper curve CPW-fed monopole antenna and circular disc CPW-fed monopole antenna.

The results of maximum total field gain vs. frequency and total gain normal to antenna plane (Z-direction) vs. frequency of these structures are shown in Figs. 11–13. From these results we can see that the space-filling CPW-fed monopole antennas have better gains in the direction perpendicular to antenna plane.

In Figs. 14–16, elevation pattern gain displays of these structures in 9 GHZ are shown. In this frequency all configurations have relatively good input matching characteristics. According to the fact that there is no ground plane except CPW ground plane, elevation pattern display in each structure is bilateral.

REFERENCES

1. Werner, D. H., and S. Ganguly, "An overview of fractal antenna engineering," *IEEE Antennas and Propagation Magazine*, Vol. 45, No. 1, February 2003.
2. Romeu, J. and Y. Rahmat-Samii, "Fractal FSS: a novel multiband frequency selective surface," *IEEE Trans. Antennas Propagation.*, Vol. 48, 713–719, July 2000.
3. Borja, C. and J. Romeu, "On the behavior of koch island fractal boundary microstrip patch antenna," *IEEE Trans. Antennas Propagation.*, Vol. 51, No. 6, June 2003.
4. Sagan, H., *Space Filling Curves*, Springer-Verlag, 1994.
5. Liang, J., L. Guo, C. Chiau, and X. chen, "CPW-fed circular disc monopole antenna for UWB applications," *proceeding of IEEE International Workshop on Antenna Technology, Small Antennas and Novel Metamaterials (IWAT2005)*, Singapore, March 2005.

The Power Line Transmission Characteristics for an OFDM Signal

A. Mori, **Y. Watanabe**, **and M. Tokuda**
Musashi Institute of Technology, Japan

K. Kawamoto
Sumitomo Electric Industries, Ltd., Japan

Abstract—In this paper, we measured what influence the sinusoidal transmission characteristics of the electric power line with various forms gave to the transmission characteristic of OFDM (Orthogonal Frequency Division Multiplexing) signal through PLC (power line communication system) modem. The electric power line transmission line with various forms in a real environment is classified into two basic elements, which are an outlet type branch and a switch type branch. Next, PHY rate (Physical rate) is measured for each basic element connected with the PLC modem. At this time, the transmission characteristics of the electric power line are simulated from measured data. OFDM sending and receiving systems are composed on the computer, and the PHY rate is simulated. By comparing with measured and calculated values, it is revealed that PHY rate of PLC modem is most affected in the case of the power line transmission characteristics having broad band and high level attenuation and is not affected in the case of that having narrow band group delay variation.

1. Introduction

Recently, Internet users are increasing by the rapid spread of the Internet and the Internet user needs the broadband that are high-rates and inexpensive communication service. While the access networks such as FTTH (Fiber To The Home) and xDSL (Digital Subscriber Line) spread, PLC attracts attention as the Internet connectivity from each room, and a home network, which controls household-electric-appliances. In PLC, since a communication network can be realized by using the existing power line, it is not necessary to install a transmission cable in addition, and a convenience outlet serves as a connection port of network at a general home, and office and factory. Moreover, since network connection and an electric power supply can be made together, we can use PLC like Wireless LAN [1–3].

However, power lines differ from telephone lines in that they are bus-type wiring and a great variety of device are connected to them. Thus, the impedance, transmission line loss and noise level of power line fluctuate greatly according to how the devices are connected and their operating conditions. To realize stable high-speed communication even under such circumstances requires the use of technology that is employed in wireless communication, such as OFDM [4, 5]. In OFDM method, it is excellent in the efficiency of the frequency use, because a lot of sub-careers are orthogonal in the frequency domain. Therefore, a lot of sub-careers can be used, and it is possible to follow to the transmission line characteristic flexibly. Moreover, in the OFDM method, when the electromagnetic wave from PLC influences other existing systems, it is possible not to use the career frequency of this band or it can be set to lower the sending level. From such a feature, the adoption of the OFDM method is a mainstream in the PLC modem [4–6].

In such a background, a real environmental test with PLC modem using the OFDM method is progressed. And, there is a report concerning the electromagnetic compatibility technology [6–9]. There are various examinations for the electromagnetic radiation characteristic and quantification method [9–12]. On the contrary, as one of the concerns for which the user uses PLC, the communication should be high-quality and be seamless in wiring in the home. If maximum 200 Mbps is achieved in the PLC modem under development without trouble, it is possible to adjust to a large data transfer of the personal computer peripherals in recent years. When paying attention to such a viewpoint, there are a lot of uncertain parts what influence the characteristic of a complex electric power line gives to the OFDM signal. In the past, the influence of the transmission characteristic of the electric power line has been verified by real environmental experiment. Therefore, the example of the quantitative examination is few.

In this paper, in such a background, we first measured the transmission characteristic of the electric power line with branch [11]. The electric power line transmission line with various forms in a real environment is classified into two basic elements, which are an outlet type branch and a switch type branch. Next, PHY rate (Physical rate) is measured for each basic element connected with the PLC modem. OFDM sending and receiving systems are composed on the computer, and the PHY rate is simulated. By comparing with measured and calculated values, we try to make clear what influence the sinusoidal transmission characteristics of the electric power line with branch gave to the transmission characteristic of OFDM (Orthogonal Frequency Division Multiplexing) signal through PLC modem.

2. Measurement of Electric Power Line Transmission Characteristic to Sinusoidal Wave Signal

2.1. Basic Elements of Power Line Transmission Model

When measuring the transmission characteristic of the power line with PLC modem, it is necessary to use shield room. However, since we have only G-TEM (Giga-hertz Transverse Electro-Magnetic) Cell, we composed the concise electric power line transmission line model as shown in Figure 1. The VVF (Vinyl insulated and Vinyl sheathed Flat type) cable with a conductor diameter of 1.6 mm is used for the power line. The electric power line transmission line with various forms in a real environment is classified into basic elements as shown in Figure 1, which are important elements influencing the power line transmission characteristics.

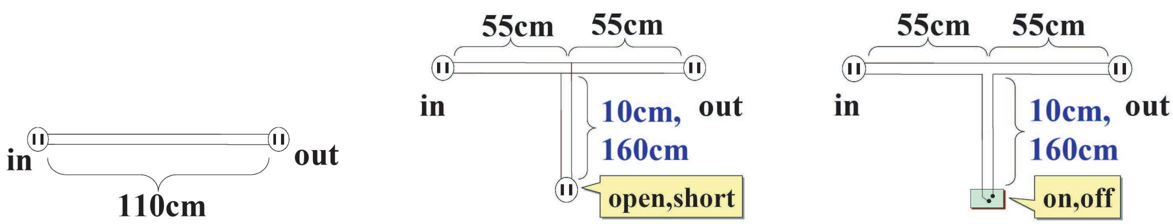

(a) No branch. (b) Outlet type branch. (c) Switch type branch.

Figure 1: Power line transmission model.

(a) No branch: The total length is 110 cm.

(b) An outlet type branch: The main cable length is 110 cm. The branch cable with length of 10 cm or 160 cm is branched at the middle point of the main cable (55 cm). The terminal form of the branch cable is open or short.

(c) A switch type branch that is used in a power line for lamp: Cable configuration is almost the same as the outlet type branch, but the branch cable is connected only one line of main cable. Terminal condition of branch cable is on or off.

2.2. Measurement of Transmission Loss Characteristics

Figure 2 shows the measurement system of the transmission loss characteristic for the basic element as shown in Figure 1 by using a network analyzer. The electric power line composing the basic element is transmission line with balance type, but a coaxial cable from the network analyzer is transmission line with unbalance type. Therefore, we used a balun at the connected point of the electric power line and the coaxial cable. The

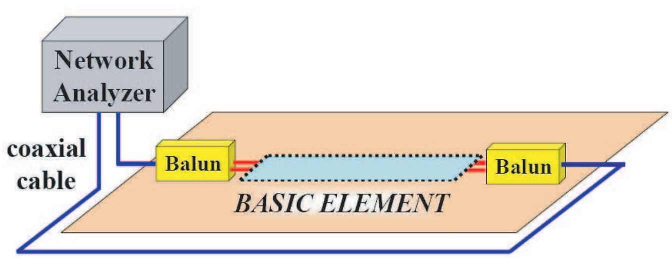

Figure 2: Measurement system of transmission loss characteristic.

measurement frequency is from 1 MHz to 100 MHz corresponding to the assurance frequency of balun.

Figures 3 and 4 show the measurement results of transmission loss characteristics for the basic element. The insertion loss of balun is subtracted from the measurement value of the transmission loss by using normalizing

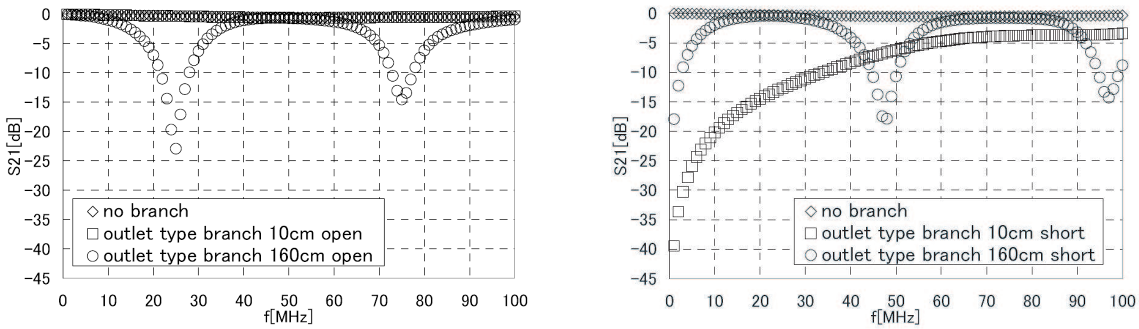

(a) Terminating condition: "open". (b) Terminating condition: "short".

Figure 3: Transmission loss characteristics of power line (Outlet type branch).

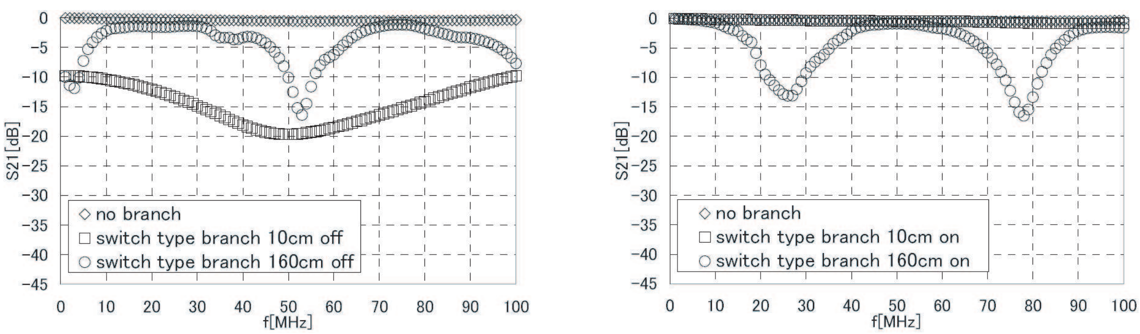

(a) Switching condition: "off". (b) Switching condition: "on".

Figure 4: Transmission loss characteristics of power line (Switch type branch).

function of the network analyzer. First, the characteristic for "outlet type branch-open" in Figure 3(a) has approached the characteristic for "no branch" by decreasing in branch length. On the other hand, sharp attenuation like the resonance appeared on the low frequency band by increasing in branch length. Especially, the transmission loss reaches up to 20 dB around the frequency of 24 MHz when the branch length is 160 cm. This band is used with the PLC modem. Next, the transmission loss for "outlet type branch-short" in Figure 3(b) becomes very large on the low frequency band according to decreasing in branch length. The transmission loss at the branch length of 10 cm became 25 dB at the frequency of 5 MHz, but the transmission loss is improved as the frequency become higher. In addition, the transmission loss at the branch length of 160 cm is not so large in all frequency band. On the other hand, the transmission loss for "switch type branch-off" in Figure 4(a) is very large in all frequency band, the maximum transmission loss reaches 20 dB around the frequency of 50 MHz when the branch length is 10 cm, because one of two lines is disconnected. But, transmission loss is improved according to increasing branch length. The transmission loss characteristics for "switch type branch-on" in Figure 4(b) are similar to that for "outlet type branch-open" in Figure 3(a) in the all frequency band.

Though this model as shown in Figures 1 is small-scale, the basic characteristics of an electric power line can be measured. Therefore, it is thought that this model is applicable as an electric power line model in the transmission measurement using the PLC modem as shown in paragraph 3.

2.3. Measurement of Group Delay Characteristic

The group delay can be calculated by the following expressions.

$$\Delta t[s] = -\frac{d\phi}{df}$$

The group delay reaches a constant value if a transmission media has a linear characteristic. Oppositely, the group delay increases if the transmission media has the nonlinearity. As an influence of the group delay to the transmission characteristic, it is considered that the guard interval length on the transmission system using

OFDM is affected by the group delay. Therefore, it is very important to understand the amount of the change of the group delay, and evaluate the transmission characteristic from such a viewpoint.

Figures 5 and 6 show the measurement result of the group delay characteristics. In the case of “outlet type branch 160 cm open” as shown in Figure 5(a), the group delay changes sharply at the frequencies of 24 MHz and 75 MHz, which correspond the frequency occurring sharp attenuations like resonance in transmission loss characteristic for the same branch condition as shown in Figure 3(a). On the other hand, in the case of “outlet type branch 10 cm short” as shown in Figure 5(b), the group delay around low frequency band does not change in spite of large transmission loss around the same frequency band as shown in Figure 3(b). And, there is a similar tendency in the case of “switch type branch 10 cm off” as shown in Figure 4(a). In this case, the transmission loss is large at all frequency band, but the group delay does not change as shown in Figure 6(a). It is clear from these results that the group delay characteristic does not relate the amount of the transmission loss, but the change of the transmission loss.

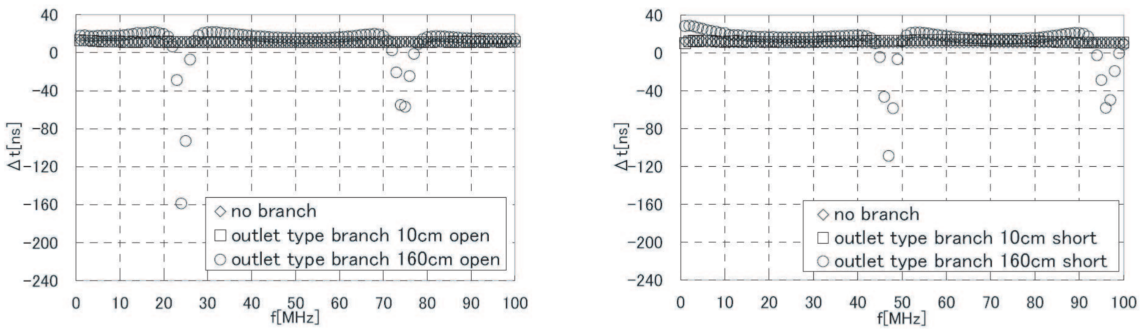

(a) Terminating condition: “open”. (b) Terminating condition: “short”.

Figure 5: Group delay characteristics of power line (Outlet type branch).

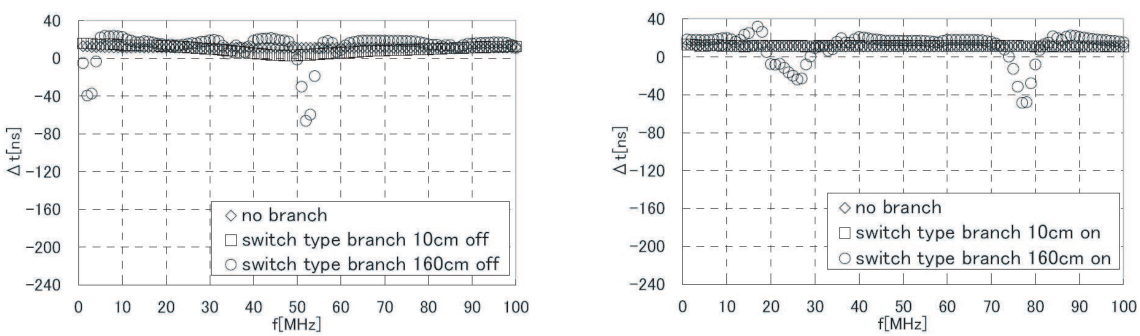

(a) Switching condition: “off”. (b) Switching condition: “on”.

Figure 6: Group delay characteristics of power line (Switch type branch).

3. Transmission Characteristics Measurement System of OFDM Signal Using PLC Modem

3.1. Measuring Method of Transmission Characteristic with Modem

We measured the transmission characteristic for the OFDM signal using PLC modem made of Sumitomo Electric Industries, LTD. Figure 7 shows the measurement system. Sending and receiving PCs is connected through the PLC modem and each model of the transmission line as shown in Figure 1. The bandwidth of the PLC modem is from 4 to 34 MHz. Next, the communication link between sending and receiving PCs through the modem is established and measured PHY rate (Physical rate). The measurement system set in a G-TEM (Giga-Hertz Transverse Electromagnetic) cell in order to suppress power supply coupling between sending and receiving modems. Normally, PLC modem is connected to AC power line, but in this case, the measurement system connected to DC power line as shown in Figure 7 is provided to suppress the power supply coupling. We considered on a grand side, and each electric power line in the GTEM Cell is set above 10 cm high from a metal floor of the GTEM cell, in order to suppress the influence of the metal floor.

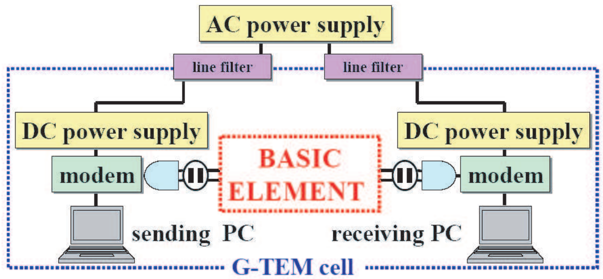

Figure 7: Transmission characteristics measurement system of OFDM signal using PLC modem.

3.2. Method of Simulating Transmission Characteristics Using PLC Modem

First, we modeled the PLC modem with the computer software and composed the OFDM sending and receiving system and simulated the transmission characteristics of the OFDM signal, that is, PHY rate for the electric power line as shown in Figure 1. Figure 8(a) shows the simulation block chart of the OFDM sending and receiving system and, Figure 8(b) shows that of the mock electric power transmission line. It is assumed that the sending and receiving systems are composed by the OFDM system based on a general FFT (Fast

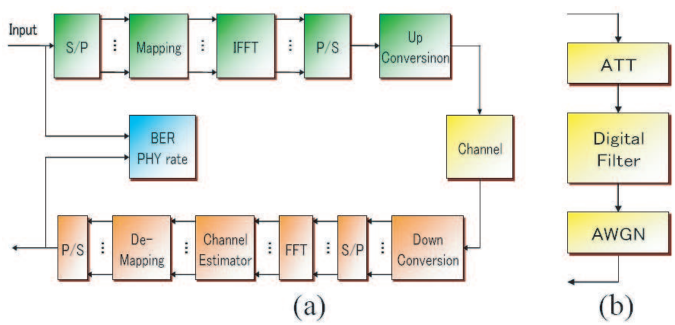

Figure 8: Simulation model of transmission characteristics for OFDM signal using PLC modem.

Fourier Transform) [13, 14]. First, the input random binary signal is converted into the frame data in the S/P (Serial/Parallel) block, and converts into a multilevel symbol by QAM (Quadrature Amplitude Modulation) in the Mapping block for each sub-career. Next, Orthogonal transform is processed in the IFFT (Inverse Fast Fourier Transform) block. As a result, base-band OFDM signal is generated, and converted into the pass-band signal by the Up-Conversion block. Here, the Channel block consists of Figure 8(b), and the composition is as follows. Wideband and constant signal attenuation are imitated in the ATT (attenuator) block. In the Digital Filter block, each electric power line is composed by using the measurement data of the transmission loss and the group delay characteristics. Moreover, the thermal noise of the equipment is imitated by the AWGN (Additive White Gaussian Noise) block. On the other hand, the receiving system is reversely converted about the sending system. The receiving signal is equalized by the Channel Estimator block. The equalization method is division of the complex number that uses the pilot-careers. Finally, the receiving binary data is compared with the sending binary data and BER (Bit Err Rate) is calculated. PHY rate is calculated from the receiving bits and the sample rate. Receiving bits are the subtraction of the error bits from all sending bits. For the simulation parameter, we calculated by using the simplified model compared with an actual modem because each parameter used for the actual modem is not obtained as public information. Therefore, the calculation of PHY rate is adjusted to measurement data when using the parameter as shown in Table 1.

3.3. Measurement and Calculation Results of Transmission Characteristic Using PLC Modem

Table 2 shows the results of PHY rate corresponding to each basic element as well as their termination conditions, and the calculated values agree well with the measured values. It became clear that basic element (b) with termination condition of "10 cm short" influences most for the PHY rate and basic element (c) with

Table 1: Simulation parameter for OFDM signal using PLC modem.

number of sub-careers	1400
first modulation	1024QAM=10 bits
use band	4 M~34 MHz
sub-career interval	43 kHz
maximum PHY rate	186 Mbps
symbol length	23 μs
guard interval length	360 ns
AWGN	S/N=50 dB

termination condition of "160 cm on" influences next. It is thought that the transmission loss was the largest in the use band of the modem. Therefore, it is clear that the transmission loss is main factor for decreasing PHY rate. On the other hand, when comparing "outlet type branch 160 cm open" with "switch type branch 160 cm on", PHY rate for "switch type branch 160 cm on" was lower. Oppositely, variable quantities of the group delay characteristic for "outlet type branch 160 cm" were larger. Therefore, it is considered that PHY rate is hardly influenced if the amount of the group delay is below guard interval length. In fact, PHY rate of PLC modem is most affected in the case of the power line transmission characteristics having broad band and high level attenuation.

Table 2: Measured and calculated results of PHY rate for PLC modem.

	PHY rate[Mbps]	
basic element and termination condition	meas.	calc.
(a) no branch	183	186
(b) outlet type branch 10 cm open	181	186
(b) outlet type branch 10 cm short	166	170
(b) outlet type branch 160 cm open	178	180
(b) outlet type branch 160 cm short	181	186
(c) switch type branch 10 cm off	180	185
(c) switch type branch 10 cm on	181	186
(c) switch type branch 160 cm off	183	186
(c) switch type branch 160cm on	168	171

4. Conclusion

In this paper, we measured and calculated what influence the transmission characteristics of the electric power line with basic element gave to the transmission characteristic of OFDM signal through PLC modem. The following items are clear by comparing with the measurement and the calculation values:

(a) The electric power line transmission line with various forms in a real environment is classified into two basic elements, which are an outlet type branch and a switch type branch. Therefore, even if a small-scale electric power line model is used, it is able to measure the characteristic of large-scale and complicated electric power line.

(b) PHY rate of PLC modem is most affected in the case of the power line transmission characteristics having broad band and high level attenuation and is not affected in the case of that having narrow band group delay variation.

In future, it is necessary to examine transmission characteristic for OFDM signal by using a complex transmission line model.

REFERENCES

1. ECHONET CONSORTIUM, "ECHONET Specification Version 2.11," ECHONET, April 2002.
2. Goldberg, G., "Evaluation of power line communication systems," *Proceedings 15th International Wroclaw Symposium on Electromagnetic Compatibility*, 103–106, June 2000.
3. Hansen, D., "Megabits per second on 50hz power lines," *Proceedings 15th International Wroclaw Symposium on Electromagnetic Compatibility*, 107–110, June 2000.
4. Matsumoto, W., "The power line communication modem by the dispersed tone modulation method which is applied multicarrier date transmission technology," *The IEICE transaction on communications*, in Japanese, Vol. J84-B, No. 1, 38–49, January 2001.
5. M. Tokuda, "Technical trends in high-speed power line communication," *The IEICE transaction on communications*, Vol. E88-B, No. 8, 3115–3120, August 2005.
6. Koga, H., N. kodama, T. konishi, and T. Gondo, "Power line communication experiment using wavelet OFDM modem," *Electronics, Information and System Society Conference*, in Japanese, OS1-1, Sept. 2004.
7. Richards, J. C., "Characterization of access broadband over power line(bpl) systems by measurements," *2005 IEEE International Symposium on Electromagnetic Compatibility, Proceedings*, Vol. 3, 982–987, August 2005.
8. Cohen, L. S., J. W. de Graaf, A. Light, and F. Sabath, "The measurement of broad band over power line emissions," *2005 IEEE International Symposium on Electromagnetic Compatibility, Proceedings*, Vol. 3, 988–991, August 2005.
9. Hare, Ed, "Measurements and calculations of bpl emissions," *2005 IEEE International Symposium on Electromagnetic Compatibility, Proceedings*, Vol. 3, 992–995, August 2005.
10. Shiozawa, H., Y. Watanabe, and M. Tokuda, "Calculation of radiated emission from the power line by 4-terminal pair network theory," *2005 IEEE International Symposium on Electromagnetic Compatibility, Proceedings*, Vol. 3, 996–1001, August 2005.
11. Miyoshi, K., N. Kuwabara, Y. Akiyama, and H. Yamane, "Calculation of radiating magnetic field from indoor ac main cable using four-port network," *2005 IEEE International Symposium on Electromagnetic Compatibility, Proceedings*, Vol. 3, 1002–1007, August 2005.
12. Watanabe, Y. and M. Tokuda, "Influence of ground plane to distance dependence of leaked electric field from power line," *2005 IEEE International Symposium on Electromagnetic Compatibility, Proceedings*, Vol. 3, 1008–1013, August 2005.
13. Triceps planning department, "Power line communication system," Triceps Co., in Japanese, 2002.
14. Triceps planning department, Triceps Co., in Japanese, 2000.

Relation Between Balance-unbalance Conversion Factor and Leaked Electric Field in Power Line with Branch for PLC

Y. Watanabe and M. Tokuda
Musashi Institute of Technology, Japan

Abstract—In this paper, we calculated balance-unbalance conversion factor and leaked electric field in the power line with branch in high frequency. We paid attention to two typical branch such as outlet branch and lamp switch branch about the branch of the electricity distribution lines, and calculated the model which is combination of those divergences. To verify the validity of the calculation, we measured the model similar to the calculation, and compared with calculation results. As a result, the measurement and calculation values were approximated well both balance-unbalance conversion factor and leaked electric field, It was shown that the calculation model in the method of moments was effective to the analysis of the power line communication. And from the comparison of the calculation results, it was shown to have good correlation between balance-unbalance conversion factor and leaked electric field.

1. Introduction

The number of Internet users has recently seen explosive growth and demand for home LAN has increased, too. The means that the network can be easily constructed domestically is demanded. As one of the some solutions, there is a high-speed power line communication (PLC). PLC transmits data by using the conventional power line laid to supply commercial electric power both inside and outside the home in stead of telecommunication line. The practical application of PLC as realization approach of Home LAN is strongly hoped with the transmission speed improving in recent years. But there is a possibility that the leaked electromagnetic wave influences a radio service of high frequency band (3–30 MHz) by using PLC, because PLC uses this high frequency band. However, there is movement to develop the leaked electric field decreasing technology and to aim for realization of PLC, because the convenience of PLC is very large. From such a background, the Ministry of Internal Affairs and Communications (MIC) inaugurated the "Study Group for Power Line Communication Facilities" in April, 2002 [1]. And, High Speed Power Line Communication Promoters' Alliance of Japan (PLC-J) was established by the Japanese electric power company and the manufacturer, and they are doing various examinations of the leaked electric field decreasing technology. Now, various experiments are conducted [2], but it is difficult to verify all cases by experimental examination. Therefore, it is necessary to study a computer calculation method that can imitate the experiment.

In an experimental examination, the leaked electric field emitted from power lines has been analyzed quantitatively by using the degree of unbalance to ground, such as Longitudinal Conversion Loss (LCL) and common mode current, as an index [3]. Thus, the simulation method that can calculate LCL, common mode current, and leaked electric field is needed. There is a method of using four port network theory [4] about the calculation method, but we focused attention on method of moments (MoM) that was one of the electromagnetic field analysis method. We thought that the calculation was easily possible in a large-scale system, so that the MoM has the feature with comparatively short calculation time.

Based on above, in this paper, we report on the result of the calculation of LCL, the common mode current distribution, and the leaked electric field in the electric power line using the MoM. And, to verify the effectiveness of the calculation, we measured the characteristics of power line system with branch under PLC-J cooperation [5]. By comparing the measurement results with the calculation one, we will clarify the effectiveness of the calculation method as well as the relation between the balance-unbalance conversion factor and the leaked electric field.

2. Power Line Model

A general domestic power line has diverged variously, but it is possible to classify it into an outlet branch and a lamp switch branch by dividing a complex divergence of each element. In the outlet branch, both two lines of a pair line composing power line is diverged to make the outlet branch as shown in Figure 1(a), but in the lamp switch branch, only one line of the pair line is lengthened to make an ON / OFF switch as shown in Figure 1(b). In this paper, we paid attention to element of branch such as the outlet branch and the lamp switch branch, and "1 branch model" connected only the outlet branch line and "2 branch model" connected both the outlet branch line and the lamp switch branch line are measured and calculated respectively.

Figure 2 shows configuration of the 2 branch model, and size of the 2 branch model is shown in Figure 3. The outlet branch line of 5.6 m in total length and the lamp switch branch line of 4.0 m in total length are connected to the backbone line like a gate form. On the other hand, in the 1 branch model, the lamp switch branch line as shown in Figure 2 is not connected. The VVF (Vinyl insulated and Vinyl sheathed Flat type) cable with a conductor diameter of 1.6 mm is used for power line. And the size of this model reduces twice from the size of actual power line system, because an actual power line system is large-scale and then it is difficult to construct the power line model in a measurement site for radiated emission. To imitate the lamp, a terminal resistor of 100 Ω is connected in the lamp switch branch line. We connected the line of 1 m in length as a switch line, and connected the switch as the terminal. There is a possibility that ON / OFF of this switch influences the characteristic of the power line. Thus, we examined the changing characteristics to switching condition of ON/OFF. Each balun terminal has lengthened line to 40 cm in the height of 20 cm as shown in Figure 4, based on regulations of the line terminal in CISPR, and this size is also reduced to half.

In order to imitate the influence of grounding one wire of the pair line in pole transformer applied to Japanese power line, we grounded one wire of the pair line in balun on opposite side of the signal impression, that is, far end side from a domestic outlet. It is a factor that one of the pair line grounding lowers the balance-unbalance conversion factor of the power line. But, the structure to extend one wire of the pair line for the switch line is also cause of unbalance in the power line. We studied the model on the side where grounded line and switch line were the same in measurement and calculation, because the combination of the same sides acts additively to the characteristic of power line.

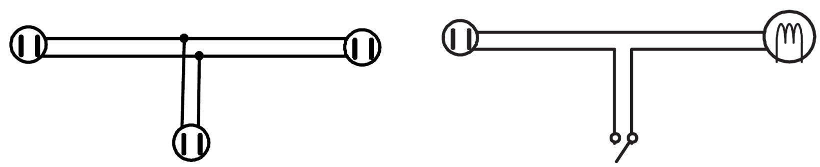

(a) Outlet branch. (b) Lamp switch branch.

Figure 1: Classification of the branch.

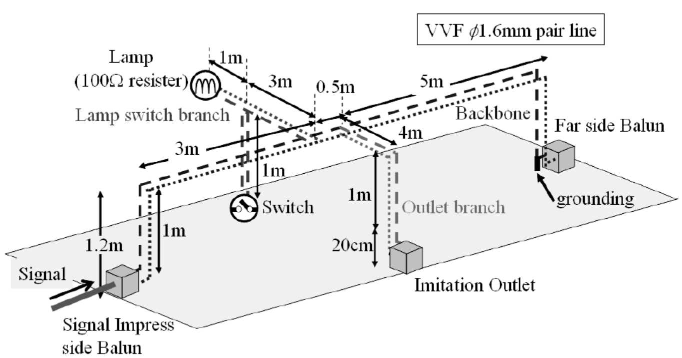

Figure 2: Configuration of the 2 branch model.

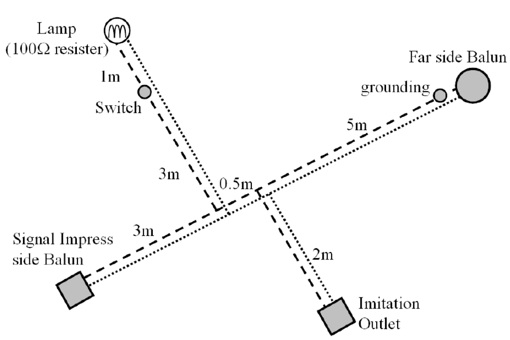

Figure 3: Size of the 2 branch model.

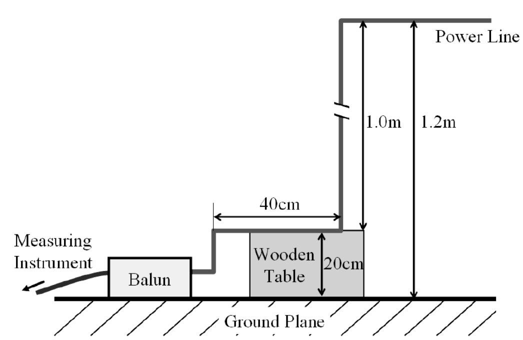

Figure 4: Configuration of power line terminal.

3. Measurement Method

3.1. LCL Measurement Method

In this paper, we paid attention to the value of balance-unbalance conversion factor, common mode current, and leaked electric field as EMC characteristics of the PLC, and measured these values and compared it with the calculation value. First, we measured LCL that was the ratio of the differential mode voltage and the common mode voltage in the input side as balance-unbalance conversion factor. LCL is defined by the following formula.

$$LCL = 20\log_{10}\frac{V_{Cin}}{Din} \quad [dB] \tag{1}$$

Here, V_{Cin} is a common mode voltage in the input side, and V_{Din} is differential mode voltage in the input side. LCL was obtained by measuring the voltage appeared in the differential mode port when impressing the signal to common mode port of the balun, by using a network analyzer as shown in Figure 5.

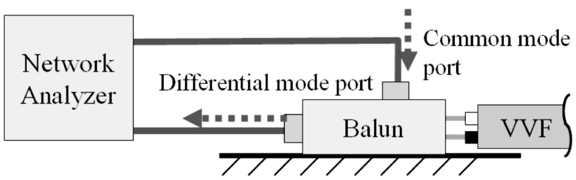

Figure 5: LCL measurement method.

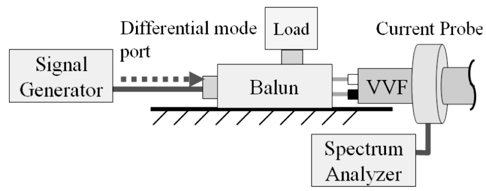

Figure 6: Common mode current measurement method.

3.2. Common Mode Current Measurement Method

We impressed the no modulated sine wave with power of 11 dBm from the signal generator to differential mode port of the balun, and measured the common mode current by using the current probe and spectrum analyzer synchronized the signal generator. Figure 6 shows the common mode current measurement system. The current distribution was obtained by measuring the current at intervals of 50 cm from signal input side balun.

3.3. Leaked Electric Field Measurement Method

In order to measure the leaked electric field from the power line, the power line model as shown in Figure 2 is set up on a large-scale turntable with radius of 5.0 m, and the no modulated sine wave signal of 11 dBm is impressed from the signal generator to differential mode port of balun. And we measured an electric field strength by a loop antenna, which is set at the point of 12 m from the center of turntable that arranged the power line model. We measured the electric field strength to horizontal, vertical and radial polarizations of loop antenna, and added all of three polarizations. The height of the antenna is 1.0 m. In the leaked electric field strength measurement, we rotated the turntable at intervals of 30 degrees. In frequency characteristics of the leaked electric field strength, the maximum value among many measured values obtained by rotating the turntable was adopted as the measured values at a frequency. Figure 7 shows the relation among arrangement of power line model and the receiving antenna position and the rotation angle of turntable.

4. Calculation Method

4.1. Calculation Model

The measurement system consisted of the power line as shown in Figure 2 was converted to an equivalent circuit of a differential transmission line to construct the calculation model by MoM as shown in Figure 8, and calculated each characteristics with MoM by using NEC2 as a calculation software [6]. Shape and size of the calculation model are completely equal to the measurement model. And we defined the model of the far end grounding by connecting the ground line of the impedance 0 Ω at far end side, because it is necessary to consider one wire grounding of pair line in the calculation model [7].

4.2. LCL Calculation Method

The electric field and magnetic field can be calculated by MoM as well as the current distribution along conductive wire, but the balance-unbalance conversion factor (for example LCL) cannot be calculated directly by MoM. However, as discussed previously, the method of simulation that can calculate LCL is demanded, because LCL is an important index of the characteristic of the power line. Thus, we devise a method of calculating LCL by the MoM. The method is shown here. First, to imitate the common mode input, we impressed the

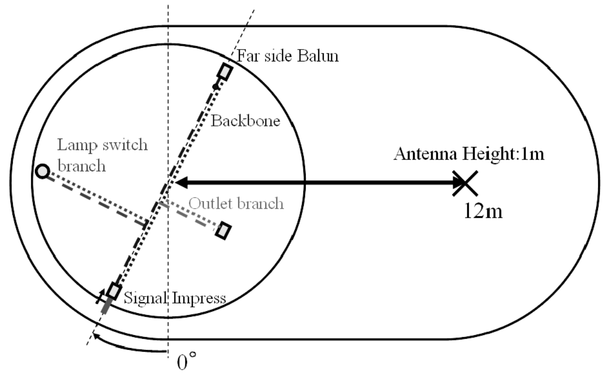

Figure 7: Configuration of power line model and receiving antenna on leaked electric field measurement systems.

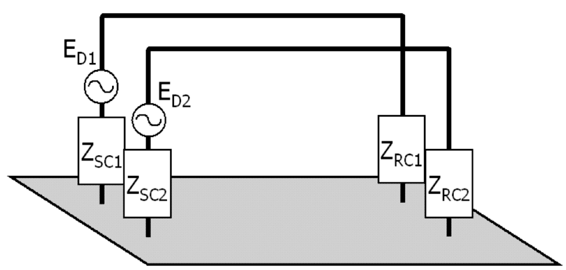

Figure 8: Calculation model by MoM.

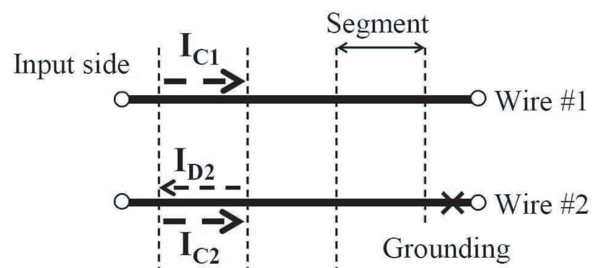

Figure 9: LCL calculation method by MoM.

in-phase voltage at the feeding point of two wires as shown in Figure 8, because LCL is a conversion ratio from the common mode signal to the differential mode signal at the input side. When grounding one wire of pair line at the far end, the current phase in an in-phase signal is greatly influenced by the grounding. Therefore, the difference of complex current appears in both lines on the segment of input side, and the subtracted value does not become 0, when one wire of the pair line is grounded on far end. This current can be considered as a differential mode current, and differential mode voltage (V_{Din}) is obtained by multiplying this differential mode current and differential mode impedance. LCL can be calculated from the ratio of V_{Din} and voltage (V_{Cin}) developed by one-quarter impedance of differential mode impedance.

4.3. Common Mode Current Calculation Method

We calculated the common mode current distribution by the method similar to the calculation of LCL, but, feeding power to each wire is impressed in reversed phase. A complex current is added to each segment at the same position of both lines, in order to calculate the common mode current distribution.

4.4. Leaked Electric Field Calculation Method

We calculated the leaked electric field at the point of 12 m from the center of power line model and 1m in height. The maximum value obtained by sweeping the angle at intervals of 30 degrees like measurement is adopted as a calculated value in calculation frequency range from 1 MHz to 30 MHz, according to the frequency range measurable by the loop antenna. And we calculated the magnetic field and converted it into the electric field by multiplying magnetic field and free space impedance.

5. Measurement and Calculation Results

5.1. LCL Calculation Result

Figure 10 shows LCL measurement and calculation results for the 1 branch model, and Figure 11 shows LCL for the 2 branch model. In Figure 10, the point is measurement value, and the solid line is calculation value. In Figure 11, Δ is measurement value for turning on switch (abbreviated as SW-ON), O is the one for turning off switch (abbreviated as SW-OFF). And the solid line is calculation value for SW-ON, the dotted line is the one for SW-OFF. From these figures, it is understood that average LCL for the 1 branch model is about 28 dB and the one for the 2 branch model is about 30 dB. In addition, it is also clear that LCL is not

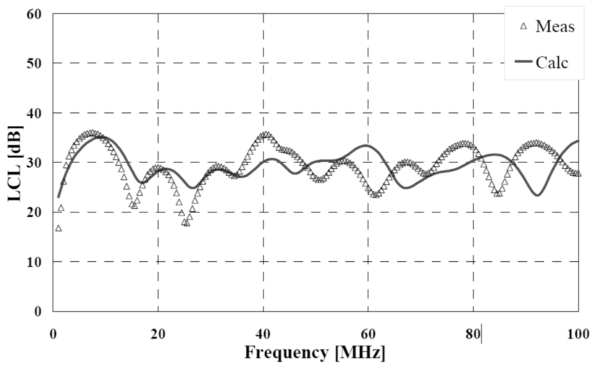

Figure 10: LCL for the 1 branch model.

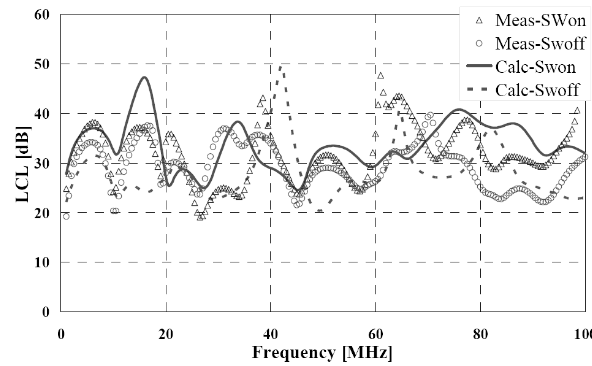

Figure 11: LCL for the 2 branch model.

so affected by switching condition, but the frequency appearing hump changes a little. From the comparison of these values, measurement and calculation values are almost corresponding though the hump position is different. The calculation value shifts the hump position to the high frequency side, and this cause is considered that dielectric constant of shielding material in each wire of the power line cannot be defined in the method of moment. Though the difference has extended in the 2 branch model, this cause is thought that the equivalent circuits for the switch and the lamp are not imitated accurately. However, it can be considered that the LCL calculation by MoM is effective, because measurement and calculation values are a similar tendency.

5.2. Common Mode Current Calculation Result

Figure 12 shows measurement and calculation values for the common mode current distribution along the backbone line in 1 branch model at frequencies of 1 MHz, 20 MHz, 40 MHz and 60 MHz. Figure 13 shows the current distribution along the outlet branch line in 1 branch model, and Figure 14 shows that along the backbone line in 2 branch model (SW-ON). The result in other cases was omitted, because the results were almost similar to that mentioned above.

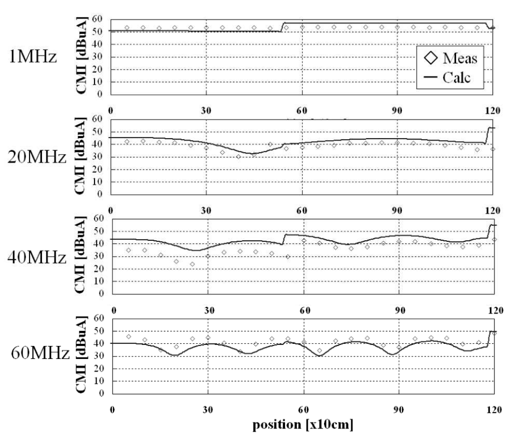

Figure 12: Common mode current for 1 branch model (backbone line).

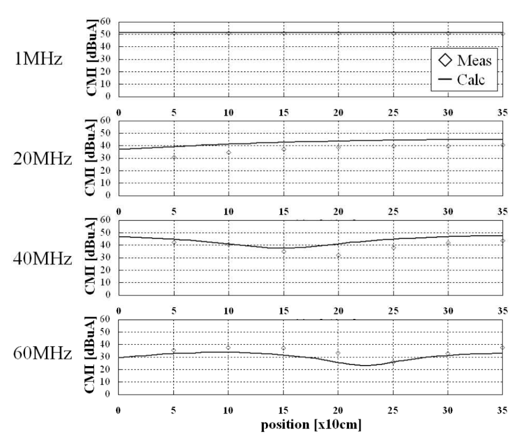

Figure 13: Common mode current for 1 branch model (outlet branch line).

From the current distribution along the backbone line shown in Figures. 12 and 13, in both the measurement and the calculation, the current has changed suddenly in 5.0 m. This position is the connecting point to each branch line and backbone line. Thus, it is understood that the common mode current flowing along the backbone line flows greatly to the line where common mode impedance is lower in the position of branch. From comparing the results, calculation values at the position of antinodes and nodes on the standing wave agree with measurement values, and the level of the common mode current is also almost equal to each other. Therefore, it was confirmed that the calculation of common mode current distribution by MoM was effective.

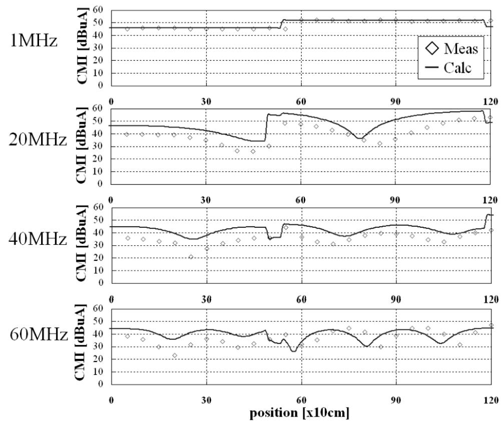

Figure 14: Common mode current for 2 branch model (backbone line).

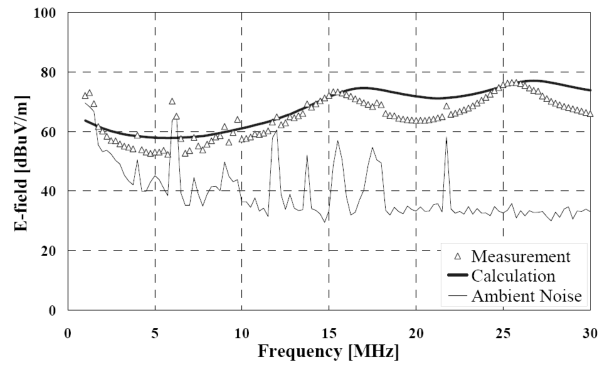

Figure 15: Leaked electric field for 1 branch model.

5.3. Leaked Electric Field Calculation Result

Figure 15 shows the value of leaked electric field for the 1 branch model. The leaked electric field for the 2 branch model (SW-ON) is shown in Figure 16, and that for the 2 branch model (SW-OFF) in Figure 17. A thin solid line in figures is ambient noise such as the broadcasting waves and noise level of the interference wave for the measuring instrument on an open area site. From those Figs. 15, 16, and 17, tendencies of the calculated frequency characteristics for the electric field strength are almost equal to measured ones. It is considered that the influence of dielectric material for power line appears as mentioned already for being a difference in the hump position, but it was revealed that the calculation for the leaked electric field by MoM was effective, because measurement and calculation values are a similar tendency.

5.4. Relation between Balance-unbalance Conversion Factor and Leaked Electric Field

Figure 18 shows a relation between balance-unbalance conversion factor and leaked electric field for the 1 branch model, and Figure 19 shows the relation for the 2 branch model. From comparing the relation between LCL and leaked electric field in these figures, if LCL reaches a low value, the leaked electric field becomes a high value, regardless of the switching condition. Conversely, if LCL reaches a high value, the leaked electric field becomes a low value. Thus, it is confirmed that there is relation of inverse proportion between LCL and leaked electric field. In addition, it is thought that such relation maintain regardless of the difference of the branch form and the switching condition.

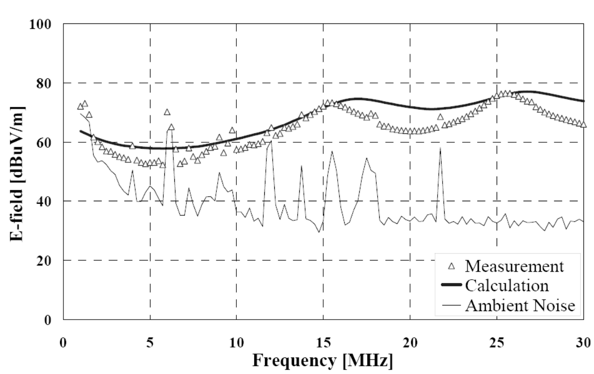

Figure 16: Leaked electric field for 2 branch model (SW-ON).

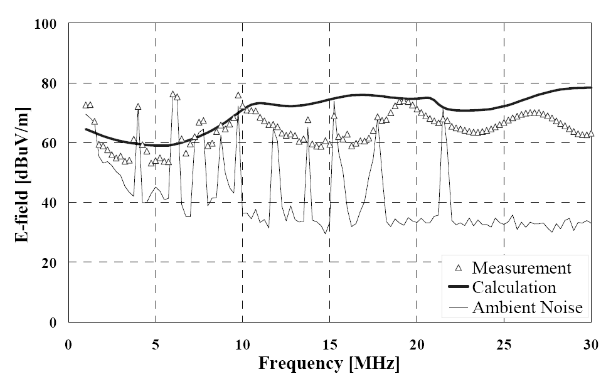

Figure 17: Leaked electric field for 2 branch model (SW-OFF).

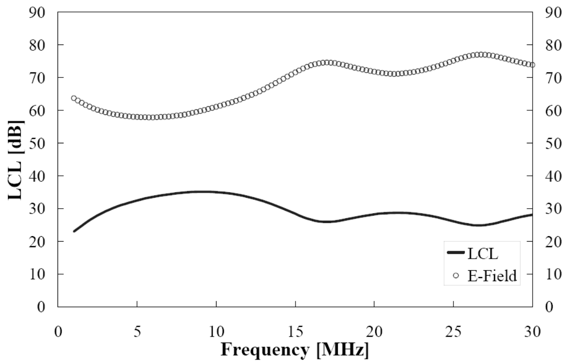

Figure 18: Relation (LCL-E-field) for 1 branch model.

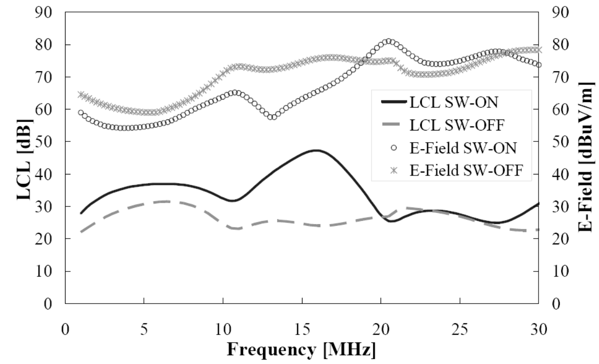

Figure 19: Relation (LCL-E-field) for 2 branch model.

6. Conclusion

In this paper, we focused attention on a power line communication using in high frequency band, and calculated balance-unbalance conversion factor and leaked electric field in the power line with branch by MoM. In order to confirm the validity of the calculation, we measured balance-unbalance conversion factor and leaked electric field for the same model as the calculation model, and compared the measurement value with the calculation value. As a result, the calculation value agreed well with measurement value, and then it was revealed that the calculation model of the PLC using the MoM was effective. In addition, it is confirmed that the influence of grounding one wire of the pair line in pole transformer applied to Japanese power line is small to LCL of the power line in the home, because LCL of the power line including each branch model is about 30 dB. Moreover, it was clear that there was a good correlation between LCL and the leaked electric field. The future task is expanding this branch model greatly, and applying it to power line model in the home.

REFERENCES

1. Power Line Communication Study Group in MIC, "Study group on Power Line Communication report," International Policy Division, International Affairs, Department Tele-communications Bureau, Ministry of Internal Affairs and Communications, Jul. 2003. (in Japanese)
2. Oka, N., A. Konemori, Y. Sasaki, H. Fukushima, M. Kato and S. Nitta, "Radiated emission from PLC and electrical unbalance of an artifical power distribution line," *2004 International Symposium on Electromagnetic Compatibility*, 4C3-2, Vol. 2, 841–844, Sendai, Japan, Jun. 2004.
3. Verpoorte, J., "Application of the LCL method to measure the unbalance of PLC-equipment connected to the low voltage distribution network," CISPR, SubCommittee I, Working Group 3 (CISPR/SCI/WG3), Feb. 26, 2003.
4. Miyoshi, K., N. Kuwabara, Y. Akiyama, and H. Yamane, "Calculation of radiating magnetic field from indoor AC mains cable using four-port network," *2005 IEEE International Symposium on Electromagnetic Compatibility, Proc.*, Vol. 3, 1002–1007, Aug. 2005.
5. Maegawa, K., N. Ishikawa, T. Shinpou, T. Inada, M. Maki, Y. Watanabe, and M. Tokuda, "Leaked electric field measurement from simplified power line model," *IEICE Technical Report*, EMCJ, EMCJ2005-67, in Japanese, 49–54, Sept. 2005.
6. http://www.nec2.org/.
7. Watanabe, Y., M. Shigenaga, and M. Tokuda, "Electromagnetic field near power line for a power line communication system," *2004 International Symposium on Electromagnetic Conpatibility*, Sendai, 4C3-3, 845–848, Jun. 2004.

Ground Wave Propagation over Complex Topography

L. B. Liu[1,2], **S. A. Arcone**[1], **and E. Rohrbach**[2]

[1]U.S. Army ERDC-CRREL, USA
[2]University of Connecticut, USA

Surface-based non LOS communication in rural areas depends strongly on the wavelength, magnitude of the relief and ground electrical properties. We are investigating the seasonal non LOS propagation of 1- GHz signals over hilly terrain with tens of meters of relief using both field observations and 3-D numerical modeling. Our objectives are to compare the modeling and measured results of relative field intensity and wavefront direction to understand the dynamics of propagation over hills and onto plateaus. The surveyed conductivity and permittivity of our site appear fairly uniform. The vegetation is mainly grass, and the surface appears fairly smooth with limited, small-scale relief superimposed on the rolling hills we mapped with GPS. We located an omnidirectional transmitter antenna in a hidden valley, and used a directional receiver antenna to measure radiation directivity at several locations, both in summer and in winter with a heavy snow cover. For computational efficiency in our model volume ($\sim 10^6\,\mathrm{m}^3$), we have temporarily lowered the frequency to 100 MHz, lowered the relative permittivity (from 16 to 9), and simplified the topography. Our field results show that waves mostly arrive in the direction of the transmitter. 2-D slices in our 3-D modeling show that the waves creep rather than diffract over the smooth hill crests. The model valleys generate multiple events, and subsurface waves are also revealed. We are presently developing propagation over the full scale topography, the temporary results of which show large scale cylindrical spreading over the relief. However, it is the details within this general picture that we will compare with the field results.

A Design of a Quadplexer Consisting of BPFs Using Different Tapped Resonators

T. Ohno
Aoyama Gakuin University, Japan

K. Wada
The University of Electro-Communications, Japan

O. Hashimoto
Aoyama Gakuin University, Japan

In the planar passive circuits, a resonator, a filter and a multiplexer are the essential key circuits in recent technical trends. In general, various studies have been conducted on out-of-band rejection and downsizing of microwave filters. It is, however, difficult to accomplish the two demands mentioned above simultaneously because of the trade-off among the number of parts, cost and simplification of the structure. If control of the number of attenuation poles is possible by a simple approach, then, it is more effective to locate the attenuation poles near the passband used for duplexers and multiplexers. To achieve the requirements above, we use a bandpass filter (BPF) based on different tapped resonators. The advantage of the proposed BPF includes the compactness, and the control of the location and number of attenuation poles.

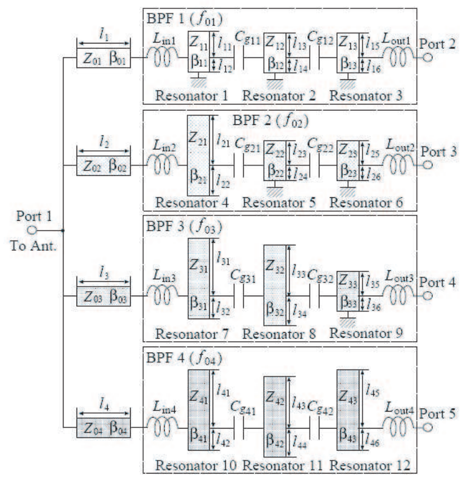

Figure 1: Schematic circuit of quadlexer consisting BPFs using different tapped resonators.

In this paper, a planar quadplexer consisting of BPFs using different tapped resonators are proposed, designed and calculated. Fig. 1 illustrates a schematic circuit of a quadplexer consisting of BPFs using different tapped resonators. In addition, Figs. 2 and 3 show the reflection, transmission and isolation characteristics of the quadplexer shown in Fig. 1. Referring to Figs. 1–3, it has been confirmed that the proposal enables the realization of the high-performance planar quadplexer theoretically.

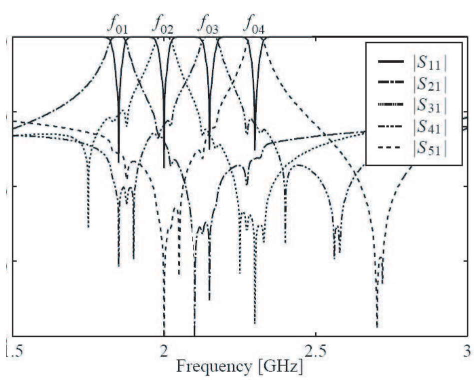

Figure 2: Theoretical results of the quadplexer shown in Fig. 1.

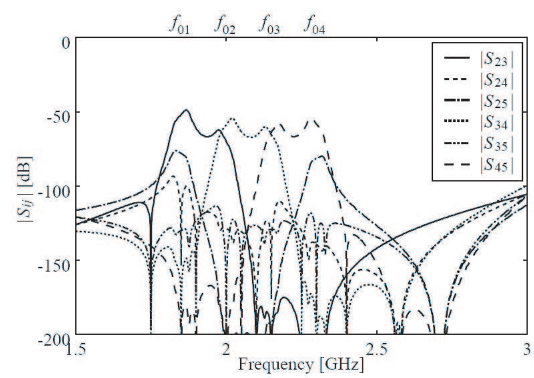

Figure 3: Isolation characteristics of the quadplexer shown in Fig. 1.

Basic Study on Relaxation of Uneven Heating in an Industrial Microwave Oven

R. Suga[1], **O. Hashimoto**[1], **T. Takatomi**[2], **T. Ijuin**[2], **and S. Watanabe**[1]

[1]Aoyama Gakuin University, Japan
[2]Daiwa Can Company, Japan

While foods are sterilized by being heated in a industrial microwave oven, uneven heating occurs inside the heated foods. This becomes a problem as the unheated part gets no sterilization and the overheated part causes deterioration of foods.

In this paper, a microwave oven was modeled based on an industrial one and model solution (starchy solution and salted starchy solution) simulated food as heated materials. Distribution of absorption power inside the heated materials in the industrial microwave oven was analyzed using parallel FDTD method, and the absorption power is substituted for heat transfer equation to analyze temperature distribution inside the heated materials. Figs. 1 and 2 show the analytical model of the industrial microwave oven used in parallel FDTD method. Figs. 3 and 1 show analysis results of temperature distribution. Refering to Figs. 3 and 1, it is confirm that parts of cup's edge is heated by the addition of sodium chloride. The tendency of the temperature distribution of the model solution was obtained and the fundamental data of the uniform appertization was provided.

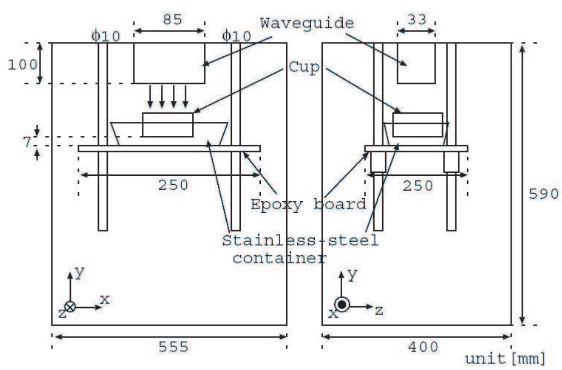

Figure 1: Analytical model.

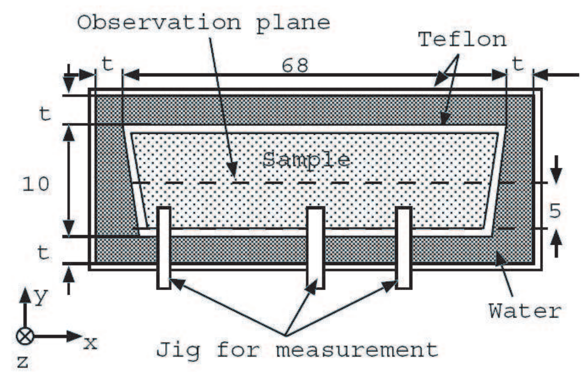

Figure 2: Cup for samples.

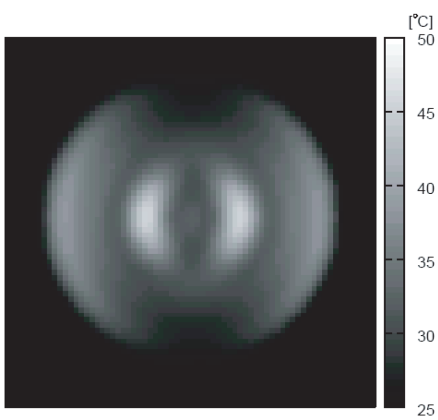

Figure 3: Temperature distribution of starchy solution (water film: 0 mm).

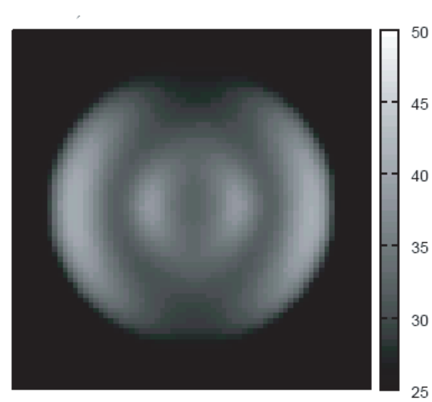

Figure 4: Temperature distribution of salted starchy solution (water film: 0 mm).

Measurement for Complex Permittivity Tensor Based on Free-space Transmission Method in Millimeter-wave Band

T. Sakai and O. Hashimoto
Aoyama Gakuin University, Japan

Rubber sheets mixed with carbon particles can be applied to wave absorbers. However, these materials usually have anisotropy which comes from the rolling method of manufacturing, because the carbon tends to be aligned along the rolling direction. So, it needs to measure complex relative permittivity tensor for the design of wave absorber in consideration of anisotropy. In this study, a measurement method which rotats sample to calculate complex relative permittivity tensor based on free-space reflection method using focusing lens and vector network analyzer is proposed.

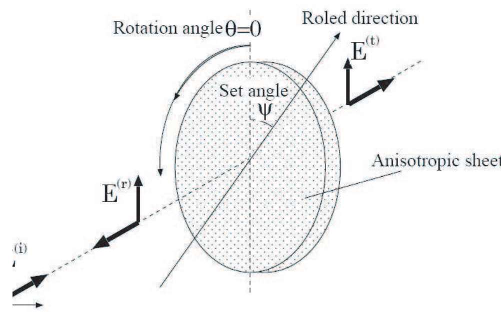

Figure 1: Analytical model.

In order to obtain the permittivity tensor of an anisotropic sheet, the transmission coefficients from these sheets must be analyzed. And the vector value of the transmission coefficients must be measured at each angle,from 0° to 180° as shown in Fig. 1. Then the permittivity tensor can be calculated by comparing the analyzed transmission coefficients with the measured values. For measurement, an anisotropic rubber sheet containing carbon particles was prepared. It was set at sample holder with rotating device and we measured the transmission coefficients in the range of 26.5 GHz to 40 GHz at only three points for each frequency.

Using above method, the values of the tensors are obtained as shown Fig. 2 and Fig. 3. It shows relativity of number of measurement points and permitivitty tensor. Then we calculate error of permittivity tensor and principal direction of tensor assuming the measurement sample theoretically. As the result, we verified that the proposed method can be used to measure permittivity tensor and principal direction of tensor.

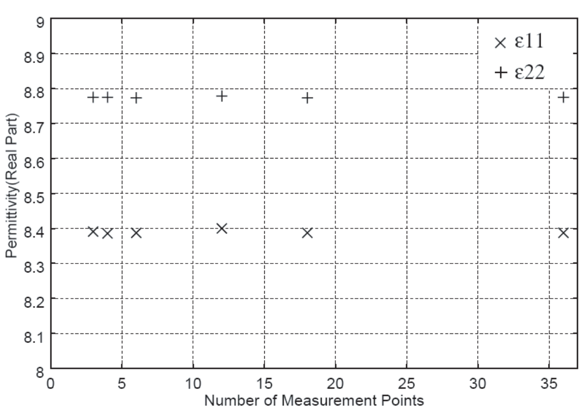

Figure 2: Real part of permittivity tensor.

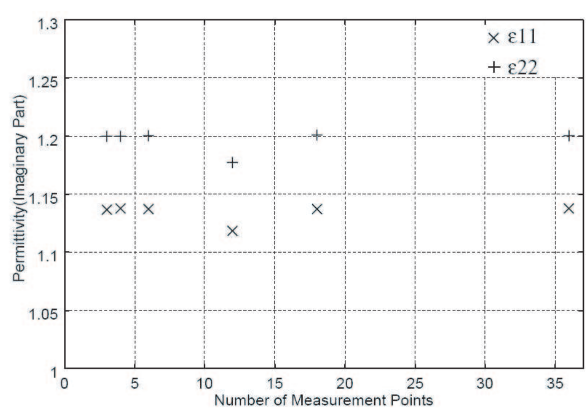

Figure 3: Imaginary part of permittivity tensor.

Analysis of Ultra-wideband Antennas for GPR Prospecting

G. Leone[1], **F. Soldovieri**[2], **R. Persico**[2], **and G. Prisco**[3]

[1]Università "Mediterranea" di Reggio Calabria, Italy
[2]Istituto per il Rilevamento Elettromagnetico dell'ambiente (IREA-CNR), Italy
[3]Seconda Università di Napoli, Italy

In recent applications in telecommunications and remote sensing at radiowaves, microwaves and terahertz frequencies, the exploitation of ultra-wideband (UWB) antennas is constantly growing up [1]. In particular, UWB antennas can provide higher imaging resolution and better target characterization in subsurface prospecting.

Design and analysis of such high-performance antennas exhibit significant challenges. In particular, in the case of GPR systems of our concern, typical requirements include not only a wide work bandwidth in order to provide short either "real" or "synthetic" pulse radiation, but also negligible interferences from undesired directions. All these features, moreover, have to be implemented in a portable systems. Still, we have to consider that, since the antennas work at close proximity or in contact with the investigated structure, their input impedance and radiated field are affected by it, so that the properties of the background medium must be taken into account in designing and analysing the antenna performance. Finally, mutual interactions between transmitting and receiving antenna must be also considered.

To directly measure the antenna properties in the operative GPR conditions, within an inhomogeneous variable scenario, is very difficult. This arises the need of a full-wave analysis of the antenna for the evaluation of its properties such as impedance, radiated field coupling, etc.

In addition, an accurate modelling of the antenna is crucial for the exploitation of inverse scattering approaches to GPR data, since the accurate knowledge of the incident field (i.e., the field impinging on the investigated zone in absence of scattering objects) is a key point to make the result of the inversion algorithm reliable.

In this contribution we present the modelling and characterization of different kind of antennas exploited in GPR applications such as bow-tie and ridged horn antennas.

The antennas are numerically analysed in different operative situations by means of the FEM-based software High Frequency Structure Simulator (HFSS), by Ansoft, which allows to model both the feeding and the radiating element of the antennas accurately.

REFERENCES

1. Hoorfar, A. and V. Jamnejad, "Electromagnetic modelling and analysis of wireless communication antennas," *IEEE Microwave Magazine*, 51–67, March 2003.
2. Soldovieri, F., R. Persico, and G. Leone, "Effect of source and receiver radiation characteristics in subsurface prospecting within the distorted born approximation," *Radio Science*, Vol. 40, No. RS3006, May 2005.